THE CAUSES OF PROPELLER PITCHING MOMENT AND THE CONDITIONS FOR ITS SIGNIFICANCE

A Dissertation
Presented to
The Academic Faculty

By

Xiaofan Fei

In Partial Fulfillment
of the Requirements for the Degree
Doctor of Philosophy in the
School of Aerospace Engineering

Georgia Institute of Technology

April 2021

THE CAUSES OF PROPELLER PITCHING MOMENT AND THE CONDITIONS FOR ITS SIGNIFICANCE

Thesis committee:

Dr. Brian J. German
School of Aerospace Engineering
Georgia Institute of Technology

Dr. Marilyn J. Smith
School of Aerospace Engineering
Georgia Institute of Technology

Dr. Dimitri N. Mavris
School of Aerospace Engineering
Georgia Institute of Technology

Dr. Nicholas K. Borer
Aeronautics Systems Analysis Branch
NASA Langley Research Center

Dr. Lakshmi N. Sankar
School of Aerospace Engineering
Georgia Institute of Technology

Date approved: April 23, 2021

Wise men learn from fools. Fools learn from no man.

?

To my wife, Yuqian.

ACKNOWLEDGMENTS

They say that a PhD is a journey of self-discovery. From the beginning, my parents have pushed me to achieve while allowing me the freedom to pursue my passions. They instilled in me a sense of standard and pride in one's work, regardless of application. In college, I was accepted by an advisor who would teach me how to learn. His patient guidance through a wide array of academic interests instructed me on the philosophy of higher education and the importance of finding my motivations. My fellow labmates at the German Research Group also taught me many of the foundational skills that I rely upon today. The past few years, I have had the honor of interning in the Aeronautics Systems Analysis Branch at NASA Langley. My mentors here show me that the impact of one's work should be greater than on oneself. Through all of this, my dear wife has supported me with immeasurable tolerance. Her dedication and kindness is a brilliant reminder of one's responsibility to others that continuously drives me to be a better person. Finally, I turn my thoughts forward to my committee members, who have graciously donated their time toward validating my efforts and are sure to challenge me in the defense ahead.

As much a journey of self-discovery, my PhD has been a discovery of family and friends. To all of you who have helped me academically, professionally, financially, and emotionally over the years, *thank you*.

This work was funded under the Transformational Tools and Technologies Project of the Transformative Aeronautics Concepts Program. A special thanks to David J. Pate, who provided the GPU-computing function for RoBIN's Biot-Savart calculations, and to Brandon L. Litherland, who provided the OVERFLOW CFD results for comparison.

TABLE OF CONTENTS

LIST OF FIGURES

SUMMARY

Recent development of vertical takeoff and landing (VTOL) aircraft has renewed interest in the study of propellers. One metric in particular, the propeller pitching moment, has been observed to be important to VTOL aircraft stability and control in the past. Propellers at angles of attack could not be accurately modeled in generations past due to a lack of computational power, but even with advances in computer technology, modern designers seem to possess insufficient knowledge in this area. In this dissertation, we study the physics behind propeller pitching moment in the context of an isolated propeller and a propeller upstream of a wing. An unsteady 3D vortex lattice method is developed specifically to model propellers at angles of attack and is validated by comparing to high-fidelity CFD analyses. We then use the model to isolate velocity influences to show that the propeller pitching moment is largely caused by two effects: a skewed wake and the presence of wing circulation. Generated maps of propeller pitching moment over a range of operational parameters corresponding to VTOL transition show that the low flight speeds and high angles of attack encountered during transition lead to significant magnitudes of propeller pitching moment that would be difficult to trim using passive methods. Also, derivation of a generalizable metric of significance shows that the peak contribution of propeller pitching moment to aircraft stability is comparable to a longitudinal displacement of the center of gravity by several percent of the wing chord. Finally, we give a concluding discussion on the impact of propeller pitching moment on VTOL aircraft design.

CHAPTER 1
INTRODUCTION

In the conceptual design of conventional propeller aircraft, thrust and torque are the primary propeller metrics of concern to the designer. Secondary effects such as the longitudinal in-plane normal force or the lateral out-of-plane yawing moment (sometimes referred to as the p-factor) may be considered if the aircraft is expected to operate beyond low angles of attack during maneuvers or during takeoff and landing, but these effects rarely constrain the aircraft design.

The recently renewed interest in vertical takeoff and landing (VTOL) aircraft has led to aircraft concepts such as tiltwings and tiltrotors that require operating propellers at much higher angles of attack during the transition from hover to forward flight. Propellers operated in this way will produce non-negligible secondary forces and moments that may compromise aircraft stability and controllability if not accounted for early in the design process. One effect in particular, the propeller pitching moment, has received little attention due to its insignificance to conventional aircraft, but we suspect that it will be important for propeller-driven VTOL aircraft based on past experimental observations.

This dissertation studies the propeller pitching moment in the context of both isolated propellers and wing-mounted propellers operating at nonzero angles of attack. A computational model is developed to investigate the underlying physics and to explore the conditions under which propeller pitching moment would be most significant to aircraft.

1.1 Background

In the mid-1900s, the US government and aviation industry made a concerted effort to research and develop VTOL aircraft. Although this effort was largely unsuccessful in realizing production VTOL aircraft, the extensive ground and flight testing performed across

multiple design programs led to valuable insights into the challenges of VTOL aircraft—chief among them, stability and control during hover and transition [1]. Of particular interest was a nose-up pitching moment during transition that was observed in concepts that required tilting the propeller, such as the Curtiss-Wright X-100 tiltprop [1] and the Vertol VZ-2 tiltwing [2, 3, 4, 5, 6]. Some deflected slipstream concepts, such as the Fairchild VZ-5 [7], also experienced pitching moment problems while others, such as the Ryan VZ-3RY [8, 9, 10], did not. Supplemental wind tunnel tests attributed the pitching moment to the propeller, which was observed to generated a pitching moment when operated at an angle to the freestream [11]. Furthermore, the pitching moment was magnified when the propeller was positioned in front of a wing [12]. The presence of this pitching moment was a hurdle for VTOL aircraft designers because established propeller models of the time were unable to predict this effect with adequate accuracy.

The aeronautics literature concerning propeller secondary effects has been (and still is) concentrated on the study of normal force and yawing moment. Works dating to as early as 1909, according to reviews by Ribner [13] and Phillips et al. [14], indicate an understanding of the advancing-retreating blade effect's role in the generation of normal force and yawing moment. One of the earliest analytical models that appropriately accounted for induced velocity was presented by Ribner [13] for propellers at small angles of yaw. De Young [15] then expanded Ribner's work to propellers at higher angles. Modern authors have continued to improve on analytical models of normal force and yawing moment [14], but the understanding of the underlying physics has remained unchanged.

In contrast, no satisfactory explanations of propeller pitching moment have been found despite multiple experiments having documented its existence [16, 17, 18, 19, 20, 21]. Early attempts to reconcile the presence of pitching moment in experimental results with the lack thereof in theoretical models led to the development of a phase lag angle model [15, 22, 23] that analogized the propeller blades to a harmonically oscillating wing. However, the phase lag angle method was shown to perform poorly when validated against

experimental results [24]. Another analytical model, by Lehman, was referenced for the propeller design of the Curtiss-Wright X-19 [25] but was also described as being inaccurate when compared to experimental data. The X-19 designers did suspect, however, that propeller secondary effects were likely strongly dependent on the induced velocity field but concluded that modeling the induced velocity field of an inclined propeller was beyond their capabilities at the time.

Perhaps an artifact of past limitations, modern propeller studies utilizing higher-order induced velocity models [26], unsteady vortex lattice methods [27], or Navier-Stokes CFD methods [28] that should be capable of analyzing propeller pitching moment still tend to omit it from discussion. Some recognition can be found in the horizontal-axis wind turbine literature [29] under the guise of lateral stability in yawed conditions, or in the quadrotor literature [30, 31], where the rotors in edgewise flight are essentially propellers at high angle of attack, but discussions are typically shallow or misguided. Description of similar effects in rotorcraft literature also exist. For example, helicopters experience a phenomenon known as "blowback" in which a nose-up pitching moment occurs upon initiating forward motion from hover [32]. However, discussions based on rotorcraft aerodynamics should be interpreted with caution because the behavior of rotors with flexible, hinged blades and cyclic pitch control may not be representative of the behavior of rigid fixed-pitch propellers.

1.2 Organization of Work

The goal of this dissertation is to answer the following two research questions:

RQ1: What are the causes of propeller pitching moment?

RQ2: Under what conditions does propeller pitching become significant for aircraft flight dynamics?

The subsequent chapters are organized as follows: Chapter 2 first posits hypotheses for RQ1 based on a first-principles analysis of the problem. Chapter 3 then details the development of an unsteady vortex lattice method tailored for modeling propellers at nonzero

angles of attack, and Chapter 4 validates said model in terms of convergence characteristics and accuracy. In Chapter 5, the developed model is used to test the hypotheses from Chapter 2 and to answer RQ1, and in Chapter 6, the model is used to explore a range of operating conditions corresponding to VTOL transition to answer RQ2. Lastly, Chapter 7 concludes with a discussion on the implications of the presented results on VTOL aircraft design.

1.3 Limitations and Definitions

The secondary propeller effects of interest to this dissertation are the resulting time-average of the blades' cyclic instantaneous loads, sometimes referred to as 1P or Aq loads[1]. The unsteady loading of individual blades is important to propeller acoustics and fatigue analysis [33, 34] but is not considered here. Additionally, the analysis herein assumes propellers to be rigid and to rotate clockwise when viewed from the aft looking forward. Figure 1.1 defines the propeller reference frame and conventions used.

Here, $-F_x$ is thrust and M_x is shaft torque. The secondary effects include F_y as the side force, F_z as the normal force, M_y as the pitching moment, and M_z as the yawing moment.

[1] 1P refers to their once-per-revolution frequency, and Aq derives from the proportionality of these loads to the product of the inflow angle, A, and dynamic pressure, q, for small inflow angles.

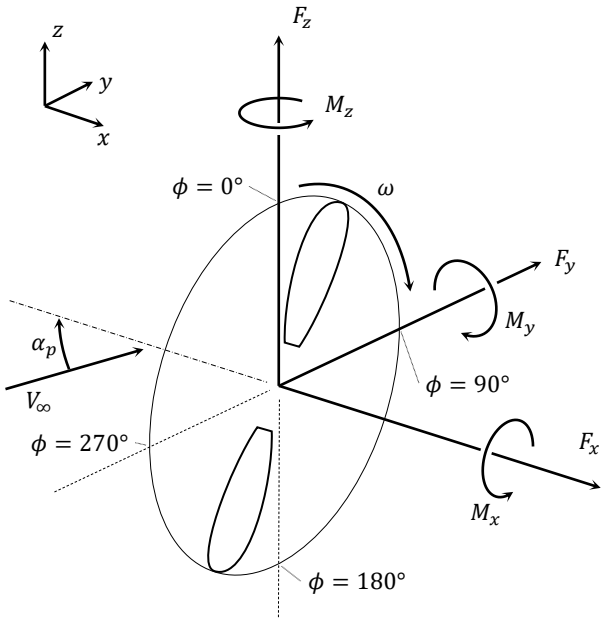

Figure 1.1: Propeller reference frame and component forces and moments generated by a propeller at an angle of attack. Arrows denote positive convention.

CHAPTER 2

HYPOTHESES FOR THE CAUSES OF PROPELLER PITCHING MOMENT

The total velocity, $\boldsymbol{V}_{tot}$, observed by a blade section of an isolated propeller can be expressed as a vector sum of components from three sources: the freestream velocity from forward motion, $\boldsymbol{V}_\infty$; the tangential velocity from propeller rotation, $\boldsymbol{\omega} \times \boldsymbol{r}$; and the induced velocity from the blades and their wakes, $\boldsymbol{V}_i$. When the propeller is at an angle of attack, α_p, defined about the y axis as illustrated in Figure 1.1, the contribution of $\boldsymbol{V}_\infty$ is not constant and varies with blade azimuthal position, ϕ. Consider the velocity diagram shown in Figure 2.1 for a generic blade section located at radius r and azimuth ϕ on a propeller at angle α_p to the freestream. The decomposition of $\boldsymbol{V}_\infty$ is given by

$$V_{\infty,x} = V_\infty \cos \alpha_p \tag{2.1}$$

$$V_{\infty,\phi} = V_\infty \sin \alpha_p \sin \phi \tag{2.2}$$

The presence of $\sin \phi$ in the magnitude of the tangential freestream velocity component, $V_{\infty,\phi}$, indicates that $\boldsymbol{V}_{tot}$ will vary with azimuthal position, resulting in unsteady cyclic loads as the blade revolves. However, if $V_{\infty,\phi}$ were the only component to vary azimuthally, then there would be zero pitching moment because the distribution of $V_{\infty,\phi}$ is symmetric about the y axis (e.g., $V_{\infty,\phi}$ at $\phi = 45°$ is identical to $V_{\infty,\phi}$ at $\phi = 135°$). Thus, for pitching moment to be nonzero, there must exist an asymmetric distribution of V_i about the y axis over the propeller disk.

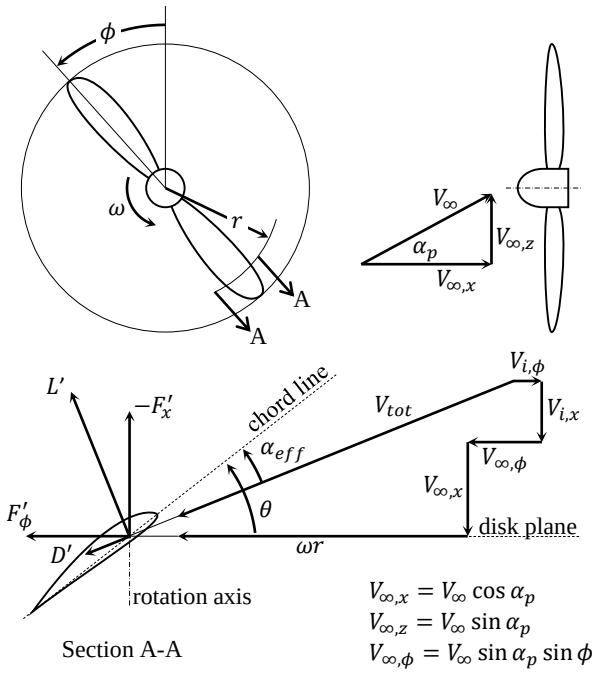

Figure 2.1: Decomposition of the total velocity at a blade section. Adapted from [14].

2.1 Skewed-Wake Effect

For the isolated propeller, consider the cases when $\alpha_p = 0°$ and $\alpha_p > 0°$, as illustrated in Figure 2.2. When $\alpha_p = 0°$, the wake structure is axisymmetric about the rotation axis and the tip vortices induce an axial component of velocity, $V_{i,x}$, in the $+x$ direction at the propeller disk. When $\alpha_p > 0°$, the wake becomes skewed in the direction of the freestream and the induced velocity distribution at the propeller disk would no longer be symmetric about the y axis. The vorticity shed from the downwind side (blue arrows) continues to induce a velocity component in the $+x$ direction at the propeller disk but is now in closer proximity to the downwind side than the upwind side. Meanwhile, the vorticity shed from the upwind side (red arrows) is now positioned to induce a $V_{i,x}$ component in the $-x$ direction on portions of the upwind side of the propeller disk. Consequently, the downwind side of the propeller disk will experience an overall larger (i.e., more positive) induced velocity component in the axial direction than the upwind side. Figure 2.3 demonstrates the aforementioned asymmetry as effected by a pair of differential vortex segments, $d\boldsymbol{l}$, that

were shed from the $\phi = 0°$ and $\phi = 180°$ positions one revolution ago. In the top diagram of Figure 2.3, the $\phi = 180°$ vortex segment points into the page, and its influence at two equiradial points on the propeller disk, P^U and P^D, results in $d\boldsymbol{V}_{i,x}^U$ and $d\boldsymbol{V}_{i,x}^D$ of opposing directions. In the bottom diagram, the $\phi = 0°$ vortex segment points out of the page, and its influence at the same two equiradial points results in $d\boldsymbol{V}_{i,x}^U$ and $d\boldsymbol{V}_{i,x}^D$ in the same $+x$ direction. However, $d\boldsymbol{V}_{i,x}^D$ is of larger magnitude than $d\boldsymbol{V}_{i,x}^U$ due to the inverse-square relationship of the Biot-Savart law with distance, s:

$$d\boldsymbol{V}_i = \frac{\Gamma}{4\pi}\frac{d\boldsymbol{l} \times \boldsymbol{s}}{s^3} \tag{2.3}$$

where Γ is the strength of vortex segment $d\boldsymbol{l}$ and $\boldsymbol{s}$ is the distance vector from $d\boldsymbol{l}$ to P. Integrating $d\boldsymbol{V}_{i,x}$ over all $d\boldsymbol{l}$ gives the aggregate effect illustrated in Figure 2.2. Note that the tangential component of induced velocity, $\boldsymbol{V}_{i,\phi}$, which is dependent on the wake helix angle, is assumed to be relatively invariant between the upwind and downwind sides of the propeller.

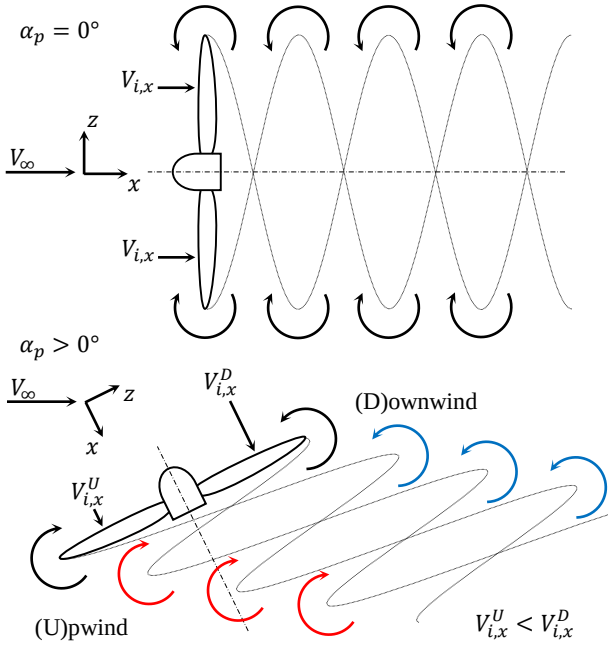

Figure 2.2: Comparison of the axial induced velocity components on a propeller at zero and nonzero angle of attack.

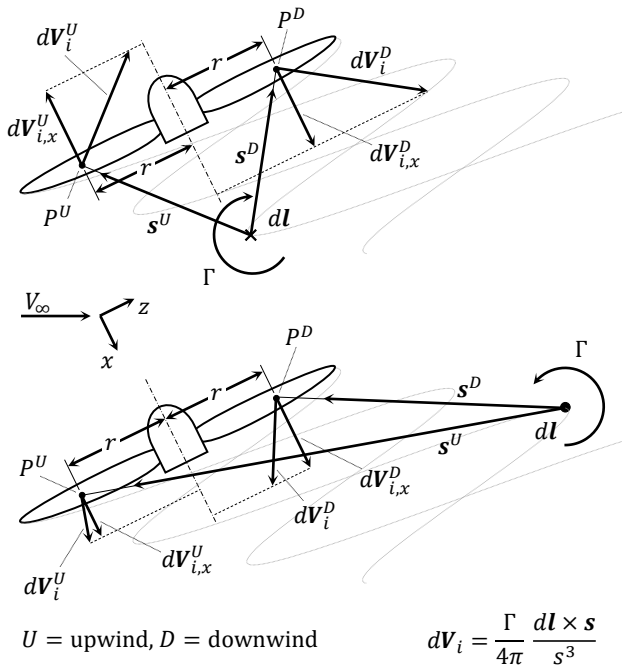

Figure 2.3: Asymmetric influence of a skewed wake on the axial induced velocity at the propeller disk.

The effect of the asymmetric distribution of $\boldsymbol{V}_{i,x}$ is shown in Figure 2.4, which depicts the velocities and sectional forces experienced by blade sections at the $\phi = 0°$ and $\phi = 180°$ positions on a propeller at $\alpha_p > 0°$. At these azimuthal positions, $\boldsymbol{V}_{\infty,\phi}$ vanishes so the only difference is due to the variation in induced velocity. A variation in $\boldsymbol{V}_{i,x}$ produces competing effects on sectional forces; increasing $\boldsymbol{V}_{i,x}$ increases the magnitude of $\boldsymbol{V}_{tot}$ but decreases the effective angle of attack, α_{eff}. In practice, the effect of α_{eff} on sectional forces is more dominant than that of $\boldsymbol{V}_{i,x}$, and thus, the blade at $\phi = 0°$ produces a lower sectional lift, L', and sectional drag, D', than the blade at $\phi = 180°$. Projection of the sectional forces in the axial direction, $-F'_x$, reveals a thrust asymmetry that would result in a positive pitching moment about the propeller origin.

Technically, a side force is also generated from the asymmetry in the sectional tangential forces, F'_ϕ, but the magnitude would be very small when compared to the propeller thrust. F'_ϕ (which is not drawn to scale in Figure 2.4) is usually at least an order of magnitude smaller than $-F'_x$, and the difference between F'_ϕ at different azimuthal positions

would be even less.

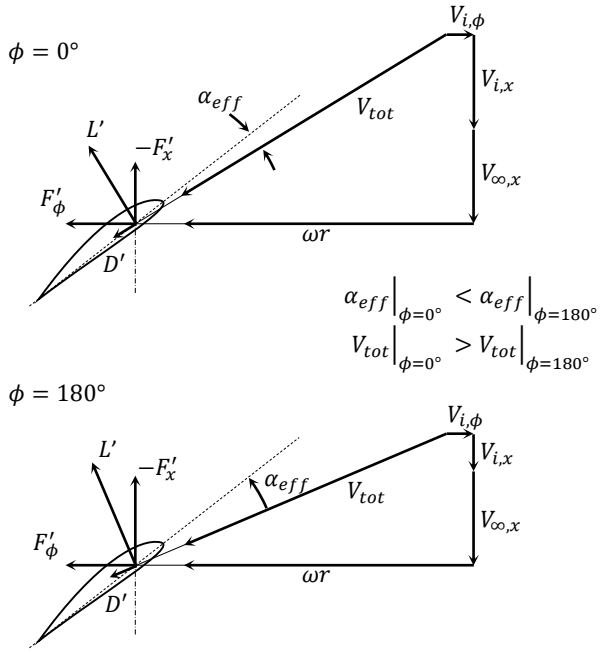

Figure 2.4: Comparison of velocity components and sectional forces on a blade section at $\phi = 0°$ and $\phi = 180°$.

2.2 Advancing-Retreating Blade Effect

For completeness, a discussion of propeller normal force and yawing moment is included here. Consider the velocities and sectional forces experienced by a blade section at the $\phi = 90°$ and $\phi = 270°$ positions on a propeller at $\alpha_p > 0°$, as depicted in Figure 2.5. At $\phi = 90°$, the blade is rotating partly against the freestream direction (i.e., advancing) such that the component of freestream velocity in the tangential direction, $V_{\infty,\phi}$, adds to the rotational velocity, ωr. In contrast, at $\phi = 270°$, the blade is rotating partly along the freestream direction (i.e., retreating) such that $V_{\infty,\phi}$ subtracts from ωr. The asymmetry in $V_{\infty,\phi}$ results in the $\phi = 90°$ position experiencing a larger α_{eff} and V_{tot} than the $\phi = 270°$ position, both of which serve to increase the L' and D' produced at $\phi = 90°$, assuming stall does not occur[1]. Projecting the sectional forces in the axial and tangential directions then shows

[1] Although it is possible for D' to decrease with increasing α_{eff} if α_{eff} is below the blade section airfoil's minimum drag angle of attack, the blades on most practical propellers would not operate in this regime.

that a positive yawing moment would be generated about the propeller origin from the difference in $-F'_x$ and that a positive normal force would be generated from the difference in F'_ϕ. In actuality, the physics are complicated by an additional asymmetry—the higher lift generated by the advancing blade results in stronger vorticity being shed and, therefore, larger induced velocity components at $\phi = 90°$ than at $\phi = 270°$. This asymmetry in induced velocity partially counteracts the effect of $V_{\infty,\phi}$ on α_{eff} and is expected to be important for the accurate modeling of normal force and yawing moment. Omittance of the asymmetric induced velocity would likely result in overpredictions of both.

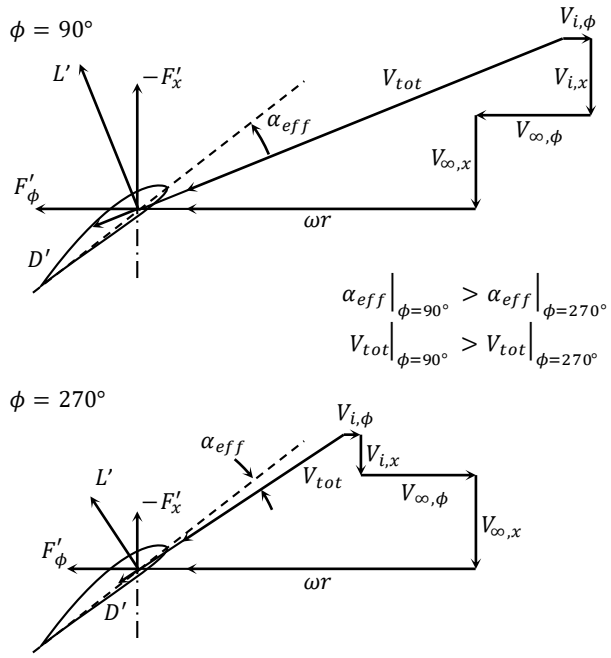

Figure 2.5: Comparison of velocity components and sectional forces on a blade section at $\phi = 90°$ and $\phi = 270°$.

2.3 Influence of a Wing

The influence of a wing behind the propeller can be inferred in a similar manner to that of the propeller wake. Figure 2.6 shows the asymmetric influence of a wing's circulation on a propeller at $\alpha_p = 0°$, where the wing is represented by a lifting line segment, $d\boldsymbol{l}$, of strength Γ pointing into the page. The induced velocities at two equiradial points on

the propeller are shown with decompositions in the x and z directions. Similar to the top diagram in Figure 2.3, the circulation about the wing results in a $\boldsymbol{V}_{i,x}$ in the $-x$ direction on the upwind side of the propeller and a $\boldsymbol{V}_{i,x}$ in the $+x$ direction on the downwind side. The effect of the asymmetric $\boldsymbol{V}_{i,x}$ on sectional forces would be similar to that described in Figure 2.4, resulting in a positive pitching moment. The circulation also induces a positive $\boldsymbol{V}_{i,z}$ over the propeller disk so the effects associated with the advancing-retreating blade effect described in Section 2.2 may be produced to some degree. If wing thickness is modeled, then an additional blockage effect would reduce $V_{i,x}$ in the immediate upstream vicinity. A propeller positioned with its hub above the wing would experience a further increase in positive pitching moment whereas a propeller mounted below the wing would see a decrease in pitching moment.

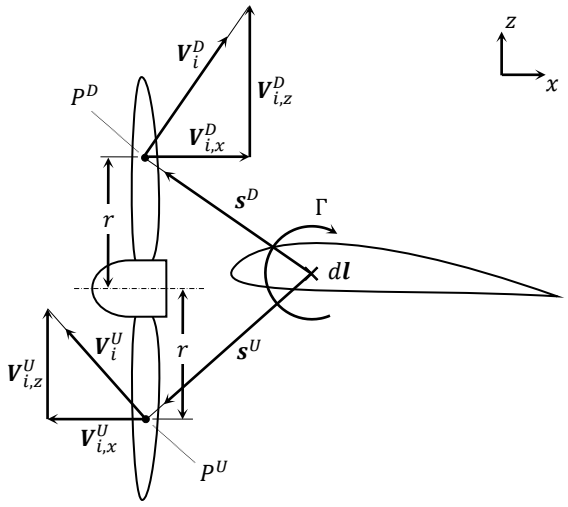

Figure 2.6: Asymmetric influence of a wing positioned behind the propeller on the induced velocity at the propeller disk.

2.4 Summary

In summary, we hypothesize that:

1) The pitching moment of an isolated propeller at an angle of attack is caused by the skewed wake generating an asymmetric axial induced velocity distribution over the

propeller disk.

2) The pitching moment produced by a propeller when positioned in front of a wing is caused by an asymmetric axial induced velocity distribution generated by the wing's circulation over the propeller disk.

CHAPTER 3
DEVELOPMENT OF AN UNSTEADY VORTEX LATTICE METHOD FOR MODELING PROPELLERS AT ANGLE OF ATTACK

Historically, vortex lattice methods (VLMs) have seen extensive use in the modeling of propellers, including conventional air propellers [35, 36], ducted fans [37], contra-rotating propellers [38], and marine propellers [39, 40]. These implementations have typically used prescribed helical vortex filament wake structures and are suitable for steady, axial flight operating conditions. However, vortex filament wake structures cannot accurately model the wakes of propellers at angle of attack. The unsteady blade loading causes vorticity to be shed in both the streamwise and radial directions, and vortex filaments would only be able to capture the streamwise component. More recently, improvements in computing speed have led to an increase in the popularity of free vortex ring wake formulations. Vortex ring elements can capture the radial vorticity [27, 41], and the free wake formulation allows for better wake fidelity under high loading conditions [42].

This chapter presents the development of a 3D unsteady VLM with free wake propagation, dubbed RoBIN (Rotating Blades at Incidence in Nonuniform flow), based on Katz and Plotkin's vortex ring formulation (found in Section 13.12 of reference [43]). Since [43] already provides a detailed discussion of the underlying theory, this chapter will focus on additions to and deviations from the original formulation. The discussion is given in the context of rotating propeller blades, but the formulation is easily extended to wings by omitting the rotational aspect.

3.1 Method Overview

A blade is represented in RoBIN as a structured grid of constant strength quadrilateral vortex rings bound to the mean camber surface. To generate this bound vortex geometry,

the physical (mean camber surface) geometry is first discretized into a structured grid with user-specified numbers of panels in the chordwise and spanwise directions. The leading segment of a vortex ring is then placed on each panel's quarter chord line, and the trailing segment is placed at the quarter chord line of the next chordwise panel. For panels at the blade's trailing edge, the trailing segment is placed somewhere in the flow behind the panel as a lump sum representation of the radially oriented vorticity shed over the last time step (or of the starting vortex in the case of $t = 0$). Katz and Plotkin suggest a location on the path of the trailing edge over the last time step at a distance 0.2-0.3 times the length of said path away from the trailing edge, and a value of 0.25 was selected for RoBIN. The side segments connect the leading and trailing segments to form a closed ring. Figure 3.1 illustrates the geometry generation process as described thus far.

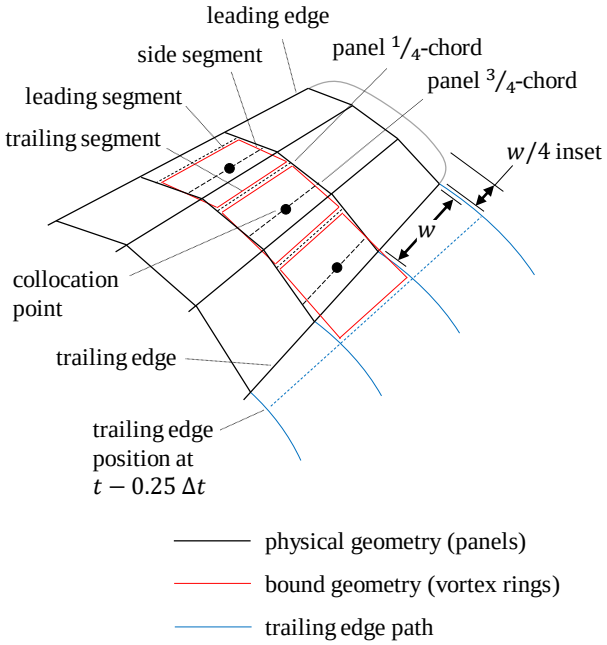

Figure 3.1: Generation of bound geometry in RoBIN.

The vortex ring strengths are solved with a system of equations that satisfies the Neumann boundary condition at a collocation point for each ring. This collocation point is located chordwise at the $^3/_4$-chord location on the respective panel and spanwise at the midpoint for uniformly spaced panels. James [44] showed this $^1/_4$-chord, $^3/_4$-chord placement

of the leading segment and collocation point, known as the Pistolesi approximation [45], to be highly accurate for its level of simplicity, and although more sophisticated placement schemes exist [46], they were not employed for the current effort.

At each time step, the geometry is first progressed by a prescribed motion, and the wake vortex rings' corner points are propagated (via the first order explicit Euler method) by the local velocities calculated at the end of the previous time step. Then, a new row of wake vortex rings is shed with strengths equal to those of the bound trailing edge rings', filling the newly formed gap between the bound and wake vortex sheets. Finally, the bound vortex ring strengths are updated, and the local velocities at the wake corner points are calculated for the next time step.

3.2 Influence Matrices

An important implication of Katz and Plotkin's suggested method for placing trailing edge trailing segments is that the bound geometry will change with blade azimuthal position when propeller angle of attack is nonzero. Specifically, the vortex rings along the trailing edge will be stretched in the streamwise direction when the blade is advancing and will be shortened when the blade is retreating because of the freestream velocity's azimuthally varying contribution to the trailing edge's path. Consequently, a unique influence matrix will be required for each unique orientation of the propeller. To limit the number of unique orientations and allow for the pre-calculation of all influence matrices, RoBIN requires a time step size such that a revolution will be completed in a whole number of time steps. Pre-calculating the influence matrices trades off computation time for memory storage, but influence matrix size has not posed a problem for the grid resolutions investigated here.

3.3 Inset Distance

In generating the bound geometry, an inset distance, illustrated in Figure 3.1, is applied at the blade tip to help increase the convergence rate of the solution with respect to grid

resolution. While the optimal inset distance depends on the load distribution over the blade [47], $w/4$ has been shown to be a good approximation for open-tipped lifting surfaces [37], where w is the spanwise width of a uniformly discretized panel. For the blade-only geometry used in Chapter 4, the inset distance was applied at both the tip and root since a spinner was not present.

3.4 Vortex Core Model

A common issue with free wake methods is that wake vortex segments can come in close proximity with each other due to wake roll up. Left alone, the nonlinearly increasing velocity influence with decreasing distance from a vortex singularity can lead to wake points experiencing unreasonably large changes in position over a single time step. RoBIN addresses this issue with a vortex core model to smooth the velocity influence in the close vicinity of a vortex segment. The model, presented by Ramasamy [48], combines a vorticity strain model by Anarath et al. [49] with the vorticity diffusion model by Bhagwat and Leishman [50]. After some rearrangement, Ramasamy's model gives the vortex core radius as

$$r_{vc}(t) = \sqrt{r_0^2 + 4\alpha_o t(\nu + a_1\Gamma)\left(\frac{l_0}{l}\right)} \tag{3.1}$$

where $r_{vc}(t)$ is the core radius at time t, r_0 is the initial core radius, α_o is the Oseen constant with a value of 1.25643, ν is the kinematic viscosity, a_1 is Squire's coefficient with an estimated value of 2e-4 based on empirical data [48], Γ is the vortex strength, l is the length of the vortex segment, and l_0 is the initial length of the vortex segment. Inside of r_{vc}, a Rankine vortex model was applied to desingularize the vortex.

Ramasamy suggests a r_0 value based on the chord length of the shedding blade section, but in practice, this approach can cause unintended side effects in VLMs. Testing showed that small enough time step sizes and panel sizes can cause the load calculation points

(see Section 3.6) or collocation points of trailing edge panels to fall inside the vortex core radius of the latest row of wake vortex segments, leading to a perpetual under-prediction of forces. Instead, r_0 was set to an arbitrary constant value small enough to exclude any locations associated with the bound vorticity at which velocities must be calculated. The r_0 value used for the presented work was

$$r_0 = 0.25 V_\infty dt \tag{3.2}$$

where dt is the time step size. In cases where a wake would intersect bound vorticity, a similar smoothing approach was applied to the bound vorticity except without any core radius growth over time. The bound vorticity was given a constant core radius equal to r_0, which prevented unreasonably large influences when intersecting previously shed wakes while avoiding an unnecessary reduction of influence on the newest row of wake segments.

3.5 Slow-start Rev-up

The prescribed motion for a propeller is a constant rotation speed combined with a constant forward velocity. If such a motion were initiated impulsively, an abnormally strong starting vortex would be created because of a lack of wake-induced downwash to reduce the effective angle of attack seen by the blade. This strong starting vortex causes increased wake deformation and must be sufficiently convected away from the propeller to achieve a steady-state solution. To alleviate the effects of the starting vortex, a slow-start rev-up scheme was implemented whereby the target rotation speed and forward velocity are achieved via a linear increase from much smaller values over a set number of revolutions (the studies presented here initiated at one percent of the target values and increased over two revolutions). Keeping the ratio of rotation speed to forward velocity constant keeps advance ratio constant and maintains the validity of the bound geometry and influence matrices, discussed in Section 3.2, over the course of the rev-up.

3.6 Load Calculation

Load calculation was performed using the Kutta-Joukowski method, which gives the total force produced by the i^{th} chordwise and j^{th} spanwise panel, $\boldsymbol{F}_{i,j}^{tot}$, as the sum of a steady and an unsteady force component:

$$\boldsymbol{F}_{i,j}^{tot} = \boldsymbol{F}_{i,j}^{st} + \boldsymbol{F}_{i,j}^{unst} \tag{3.3}$$

The steady force component, $\boldsymbol{F}_{i,j}^{st}$, is given by

$$\boldsymbol{F}_{i,j}^{st} = \rho_\infty(\Gamma_{i,j} - \Gamma_{i-1,j})(\boldsymbol{U}_{i,j} \times \boldsymbol{l}_{i,j}) \tag{3.4}$$

where $\Gamma_{i,j}$ is the strength of the vortex ring associated with panel i, j, $\boldsymbol{l}_{i,j}$ is the vector of said ring's leading segment, and $\boldsymbol{U}_{i,j}$ is the local total velocity calculated at the midpoint of the leading segment. Equation 3.4, in effect, combines the steady force contributions of ring i, j's leading segment and the upstream ring's trailing segment. For panels at the leading edge, the strength of the upstream ring, $\Gamma_{i-1,j}$, is set to zero. For panels at the trailing edge, the equation is unchanged, but note that there is no contribution from the trailing segment because it is technically part of the wake and should be force-free.

Consistent with many other VLM implementations [41, 51], Equation 3.4 calculates the force from only the bound spanwise-oriented vorticity contained in the leading and trailing vortex segments. Such an approach derives from the assumption that the flow at any point along a blade is two-dimensional and normal to the spanwise direction. The bound chordwise-oriented vorticity of the side segments would then be aligned with the flow and produce no appreciable force. This assumption is generally valid for wings in forward flight or for propellers normal to the freestream but not necessarily for propellers at a nonzero angle of attack. For example, a blade at $\phi = 0^\circ$ or $\phi = 180^\circ$ on a propeller at $\alpha_p > 0^\circ$ is effectively at a negative angle of attack with respect to $\boldsymbol{V}_\infty$, and a vortex ring on the blade would be oriented with its side segments normal to $\boldsymbol{V}_\infty$. The leading and trailing

segments will still account for a majority of the total force (being mostly normal to the dominant rotational velocity, $\boldsymbol{\omega} \times \boldsymbol{r}$) but the contribution from the side segments may not be negligible. Some references [52, 53] have suggested that unsteady VLMs should apply Equation 3.4 to all of the segments of a vortex ring for better accuracy. However, for the test case described in Chapter 4, load calculations that included steady force contributions from all bound vortex segments were less accurate than those made with the established spanwise-only method, especially for side and normal force.

The unsteady force component, $\boldsymbol{F}_{i,j}^{unst}$, is given by

$$\boldsymbol{F}_{i,j}^{unst} = \rho_\infty \frac{\partial \Gamma_{i,j}}{\partial t} A_{i,j} \frac{\boldsymbol{U}_{i,j} \times \boldsymbol{l}_{i,j}}{|\boldsymbol{U}_{i,j} \times \boldsymbol{l}_{i,j}|} \tag{3.5}$$

where $A_{i,j}$ is the area of panel i, j. According to Cole [51], there are two interpretations of the unsteady force component which agree in magnitude ($\rho_\infty \frac{\partial \Gamma_{i,j}}{\partial t} A_{i,j}$) but differ in directionality. The first is seen in a work by Drela [54] and is applied in the local lift direction, normal to the local total velocity; the second is seen in works such as [52, 53] and is applied in the panel normal direction. After testing both directions, applying the unsteady force component in the lift direction was found to produce more accurate results. These findings support Katz and Plotkin's [43] remark that a normal force based solely on the pressure difference across the vortex ring overpredicts the induced drag by not capturing the suction peak.

When aggregating propeller forces, the individual force components can be summed and decomposed into directional components without regard for their point of application. When calculating propeller moments, the force components were applied at their respective leading segments' midpoints.

CHAPTER 4
MODEL EVALUATION

A series of studies were performed to evaluate RoBIN's accuracy and convergence characteristics with respect to simulation time, grid resolution, and time step resolution. The convergence studies were conducted using an isolated propeller geometry, and accuracy was tested for both an isolated propeller and a propeller upstream of a wing.

4.1 Geometry

The high-lift propeller (HLP) of the NASA X-57 Maxwell [55] was used as the test propeller because the exact geometry was known and CFD analyses of the blades without a spinner were readily available. The HLP has a radius of $R = 0.2880$ m, five blades with a constant MH 114 airfoil along the radius, and the geometry distributions shown in Figure 4.1 [56]. All studies were conducted at the HLP design condition of 4550 rpm, $V_\infty = 29.8$ m/s (58.0 kts), and $\rho_\infty = 1.225$ kg/m^3. The propeller origin about which moments were taken was defined as the intersection of the blade stacking axes and the rotation axis.

For the propeller and wing case, a cross section of the X-57 wing was extruded to form a rectangular wing. The wing has a span of 3.048 m (10.00 ft) and a chord of 0.7142 m (2.343 ft). The wing was positioned with its midspan quarter-chord at [X, Y, Z] = [0.437315, 0, 0.108] m ([1.43476, 0, 0.353] ft) relative to the propeller origin and with its chord plane parallel to the propeller's x-y plane. The midspan quarter-chord was the reference point for wing moments. Figure 4.2 shows the propeller and wing geometry as modeled in RoBIN.

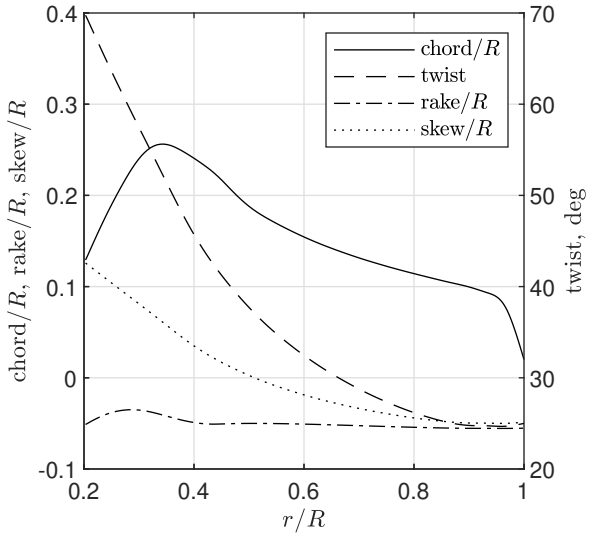

Figure 4.1: HLP blade geometry.

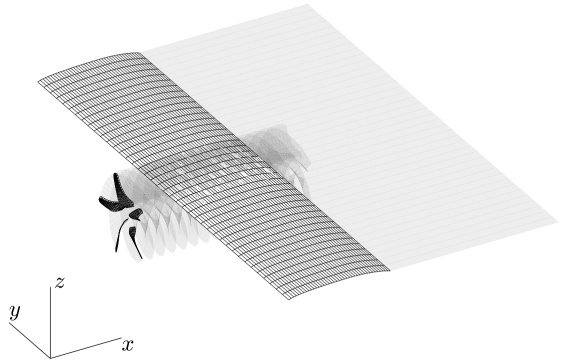

Figure 4.2: X-57 HLP and wing as modeled in RoBIN visualized with a notional prescribed wake.

4.2 Simulation Time Convergence

The first study investigated RoBIN's convergence behavior with respect to simulation time, measured in number of revolutions, N_{rev}. The geometry was discretized into 20 spanwise and chordwise panels per blade, and a time step size corresponding to $\Delta\phi = 5°$ (72 steps per revolution) was chosen. Figure 4.3 shows the moving average of the forces and moments over the last revolution for a wide range of α_p. Although most runs converged smoothly, there exists an unsteadiness in the results that grows to a visually observable

magnitude by the $\alpha_p = 60^\circ$ case. The unsteadiness is due to increasingly strong distortions in the wake, as demonstrated in Figure 4.4. The inclusion of a vortex core model helped to avoid the worst of the singularity-related instabilities, but the wakes of loaded propellers will inevitably accumulate more curvature than what its fixed grid resolution can accurately model. This can lead to unrealistic stretching, improper wake intersection, and a general loss of geometric fidelity. Attaining cleaner convergence behavior at higher α_p would require a dynamic wake refinement algorithm. The study was repeated for coarser and finer grid and time step resolution settings with similar results.

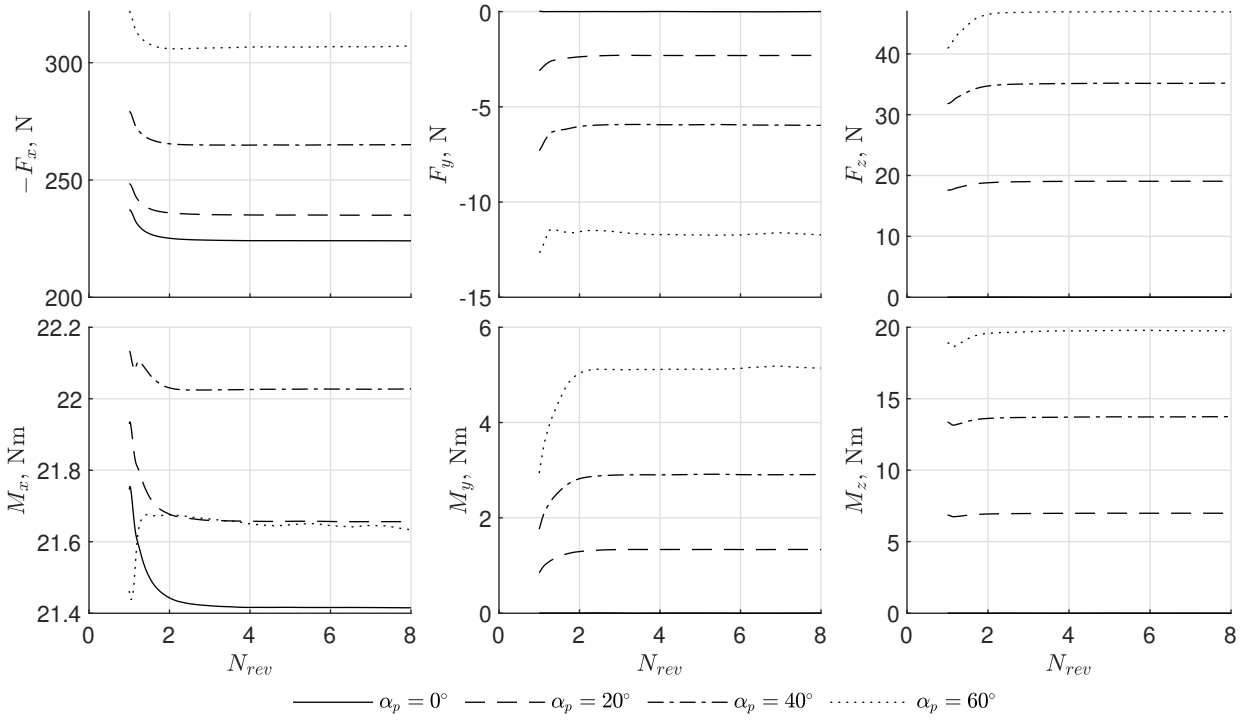

Figure 4.3: RoBIN convergence behavior with respect to number of revolutions.

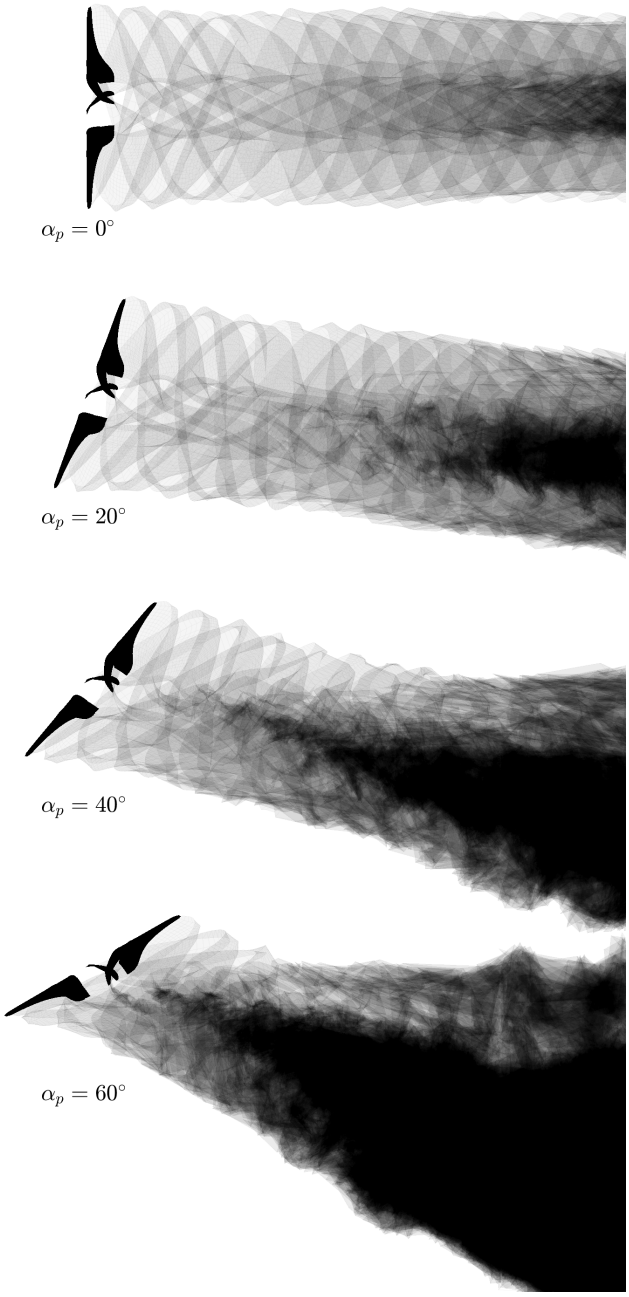

Figure 4.4: Demonstration of increasingly strong wake distortions with propeller angle of attack.

4.3 Grid Resolution and Time Step Resolution Convergence

The second study investigated RoBIN's convergence behavior with respect to grid resolution and time step resolution. Grids were constrained to have the same number of chordwise and spanwise panels, and the time step sizes were constrained to result in a whole number

of steps per revolution. Figure 4.5 shows the convergence behavior with respect to grid resolution, measured in number of panels per blade, N_{ppb}, and Figure 4.6 shows the convergence behavior with respect to time step resolution, measured in number of time steps per revolution, N_{tpr}. The values shown are for $\alpha_p = 30°$ and are the average forces and moments over the last revolution normalized by their respective CFD predictions, denoted by an asterisk (CFD results are discussed in Section 4.4).

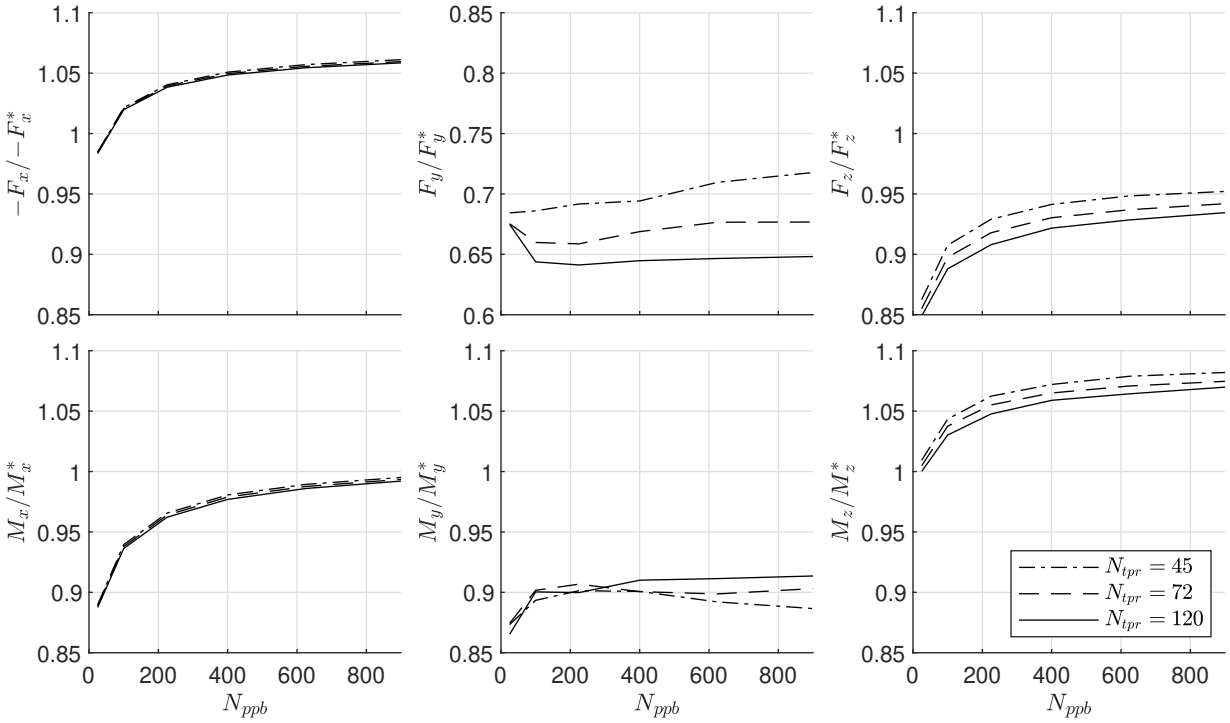

Figure 4.5: RoBIN convergence behavior with respect to grid resolution. $\alpha_p = 30°$.

Overall, the convergence is well behaved with most metrics asymptoting towards values within 10% of the CFD predictions. F_y and M_y show the most difficulty in converging with both measurements seeming to fluctuate from what would be a smooth convergence curve. Upon closer inspection, these fluctuations are present for all other forces and moments but are imperceptible when compared to the magnitudes of their unnormalized values. Based on this observation, these fluctuations are likely caused by the same wake distortions discussed in Section 4.2 because F_y and M_y are primarily caused by a wake-induced velocity asymmetry that, unlike F_z and M_z, is not diluted by the asymmetry in tangential freestream

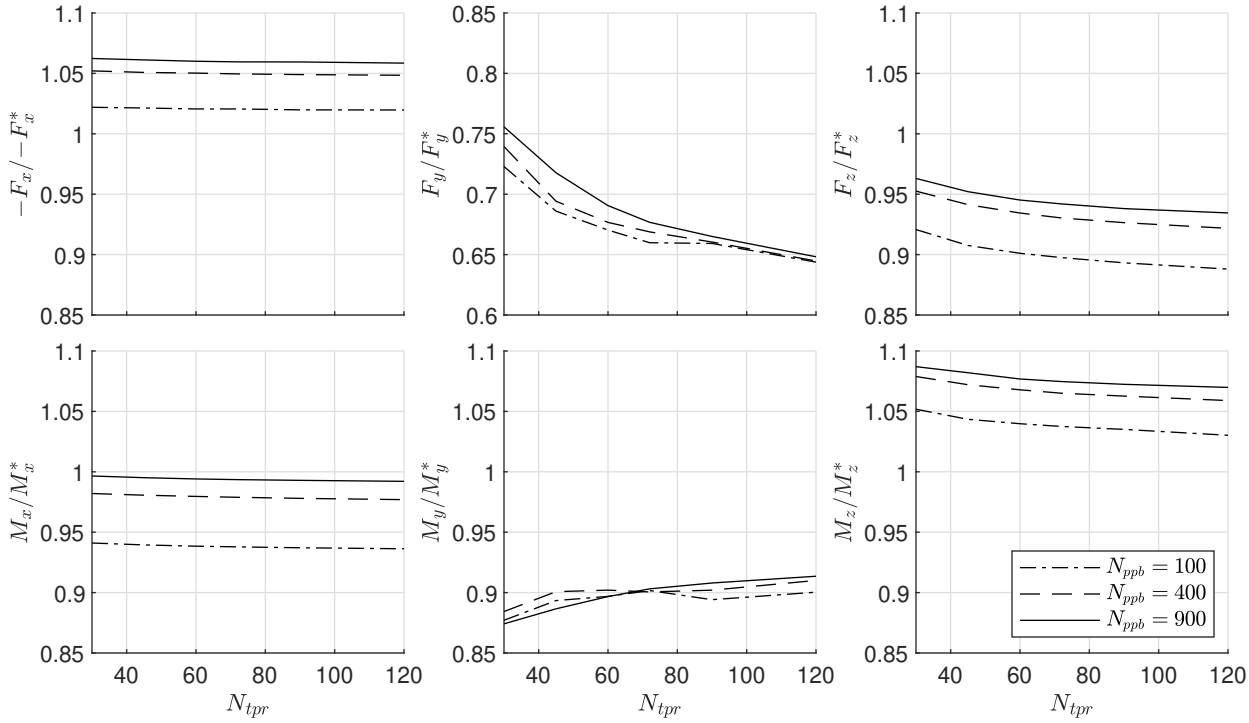

Figure 4.6: RoBIN convergence behavior with respect to time step resolution. $\alpha_p = 30°$.

velocity. The 25-35% underprediction in F_y is due to the small magnitude of F_y^*. The impact of any inaccuracy, such as the lack of viscous drag, is exaggerated in the prediction of F_y.

F_x and M_x are especially insensitive to N_{tpr} because increasing N_{tpr} has little effect on the total amount of vorticity in the wake and, therefore, little effect on the average velocity induced by the wake at the propeller disk. The increase in each measurement with N_{ppb} is at least partly due to the inset distance shrinking as the panel size decreases, resulting in larger modeled blade areas.

4.4 Accuracy Compared to CFD

RoBIN's accuracy was evaluated by comparing against CFD analyses. The primary reason for using CFD instead of experimental data was the ability to exclude the nacelle and spinner, which have been shown to generate side and normal forces comparable in magnitude to those of the blades [57]. Since the mean camber surface representation in VLMs is unsuit-

able for modeling thick bodies, a blade-only geometry was more appropriate for evaluating RoBIN's accuracy. The CFD software used for the evaluation was OVERFLOW.

4.4.1 OVERFLOW Setup

The model geometries were created using Open Vehicle Sketch Pad (OpenVSP) [58] and exported in a PLOT3D format for gridding. Chimera Grid Tools (CGT) [59] was used to assemble the overset grid systems. The final grid systems were saved as unformatted, double-precision, big endian multigrid files for analysis in OVERFLOW.

OVERFLOW (OVERset grid FLOW solver) is a structured, overset grid, Reynolds-Averaged Navier-Stokes, CFD flow solver developed at NASA [60, 61]. A fifth-order WENO5M (Weighted Essentially Non-Oscillatory) method [62] with HLLE++ (Harten, Lax, van Leer and Einfeldt) flux scheme [63] was used to calculate inviscid flux contributions and second-order central differences were used to approximate the viscous flux. A k-ω SST-RC-QCR2000 (rotation correction with quadratic constitutive relationship) turbulence model [64, 65] coupled with the Langtry-Menter CFX-v-1.1 transition model [66], despite not being Galilean invariant, was used to maintain commonality with previous X-57 studies [55, 56]. This method has been successfully used in other situations with rotational reference frames, e.g., Jain [67, 68]. The propeller analyses used dual time stepping with 20 subiterations and a physical step size corresponding to 1° of rigid body rotation to predict the time accurate flow field, with at least eight revolutions of propeller travel being simulated. Total forces and moments were then averaged over the final revolution.

To obtain radial and azimuthal distributions of blade forces and moments, solution files were generated every 12 degrees following the eighth propeller revolution. The force and moment distributions were computed along each blade at each position using the TRILOAD program [69]. TRILOAD slices a triangulation of surface loads into many bins defined by a binning direction and distance and then outputs the resulting bin loads into an output file. The binning direction for each flow solution was defined such that each bin

slice was perpendicular to the blade spanwise direction. Blade section loads were computed using 100 uniformly spaced bins between the blade root and tip.

4.4.2 Angle of Attack Sweep for Isolated Propeller

Figure 4.7 shows the comparison of RoBIN vs. OVERFLOW isolated propeller results over a sweep of α_p. For these runs, the geometry was discretized into 20 spanwise and chordwise panels per blade ($N_{ppb} = 400$), the time step size corresponded to $\Delta\phi = 5^\circ$ ($N_{tpr} = 72$), and the simulations were run until $N_{rev} = 6$.

RoBIN's predictions show good agreement with those from OVERFLOW until stall begins to occur in the OVERFLOW solutions at $\alpha_p = 40^\circ$. The stall occurs in the upwind region, and the loss of lift there causes a sharp departure in predicted M_y and a corresponding departure in predicted $-F_x$. Prior to stall occurring, $-F_x$ predictions from RoBIN are approximately 5% larger than OVERFLOW's predictions. This overprediction is likely due to a combination of lacking viscous drag in the axial direction and a discrepancy between the inviscid and viscous lift curve characteristics of the MH 114 airfoil. As shown in Figure 4.8, the viscous lift curve of the MH 114 airfoil is slightly lower than the inviscid lift curve[1] due to Reynolds number effects. The viscous lift curve also gradually stalls so regions of the blades at $\alpha_{eff} \gtrsim 5^\circ$ overpredict lift and, consequently, thrust more in RoBIN. The discrepancy in lift curves also causes RoBIN's M_z predictions to be approximately 5% higher than those from OVERFLOW. Since the advancing blades experience higher α_{eff} than the retreating blades, the advancing side sees a greater overprediction of thrust, resulting in a higher M_z prediction from RoBIN.

RoBIN's underprediction of F_z is not entirely unwelcome. The recognized lack of viscous drag effects in RoBIN should result in an underprediction of F_z because the presence of a $V_{\infty,z}$ component in the $+z$ direction would produce a corresponding net parasitic drag force in OVERFLOW. RoBIN's F_y predictions are also thought to be reasonable consider-

[1]The inviscid lift curve was generated by modeling a wing with an aspect ratio of 1000 and extracting the forces from the middle section.

ing the lack of viscous effects.

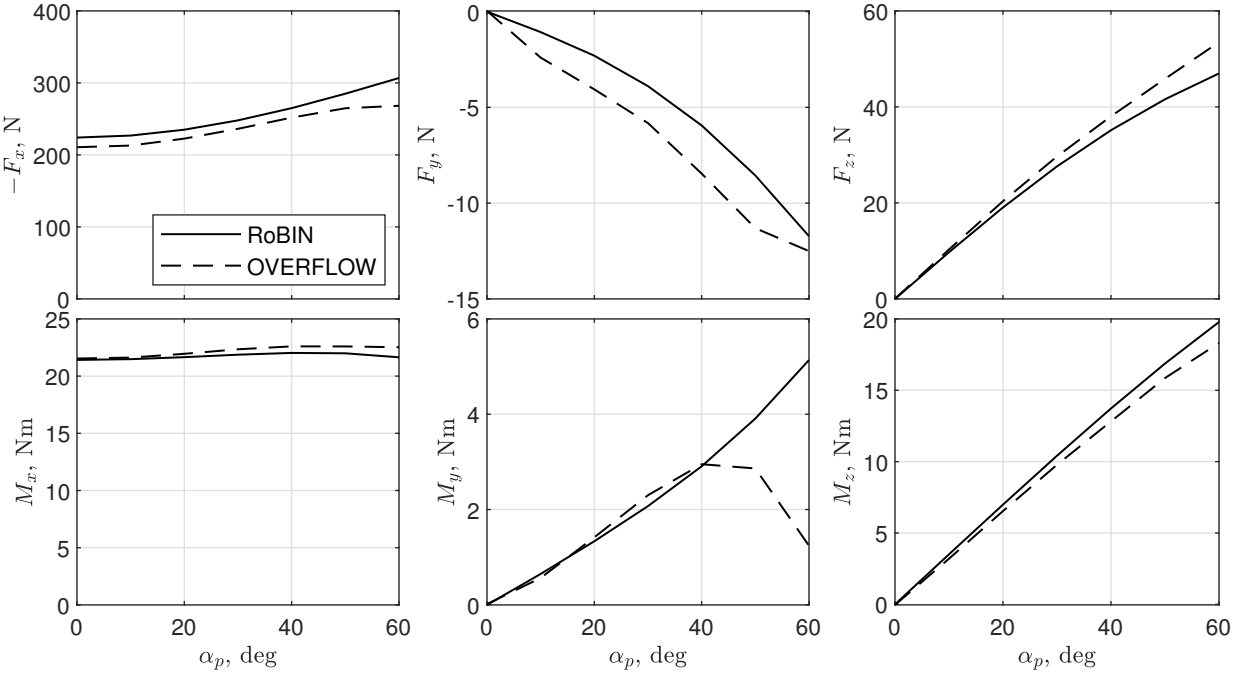

Figure 4.7: Comparison of RoBIN and OVERFLOW results for the isolated HLP over a sweep of α_p.

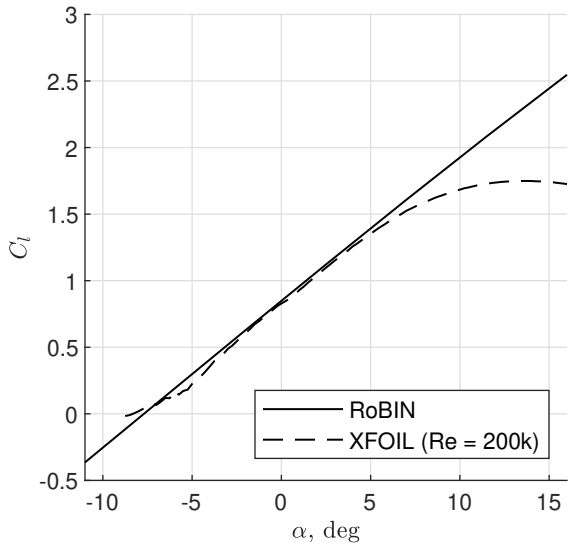

Figure 4.8: Comparison of inviscid (RoBIN) and viscous (XFOIL) lift curves for the MH 114 airfoil.

4.4.3 Force Distribution Comparisons

For a more in-depth analysis of the errors observed, Figure 4.9 compares contours of sectional thrust, $-F'_x$ and $-F'^*_x$, from RoBIN and OVERFLOW, respectively, overlaid on a colored map of the dimensional error, $-F'_x - (-F'^*_x)$ for $\alpha_p = 30°$. The extra lift resulting from the inviscid lift curve discussed previously is evident by the general overprediction over most of the disk, and the enlarged RoBIN contours on the advancing side confirm that the discrepancy is more pronounced there. Interestingly, the region of highest (dimensional) error—the tip region between approximately $\phi = 30°$ and $\phi = 90°$—is not aligned with the peak loading direction of $\phi \approx 105°$, indicating that its cause is likely not related to the discrepancy in lift curves. Figure 4.10 shows the same $-F'_x$ and $-F'^*_x$ contours as Figure 4.9 but overlaid on a colored map of the normalized error, $\frac{-F'_x-(-F'^*_x)}{-F'^*_x}$. When normalized, the region of highest error is revealed to be a band of overprediction at the tip between $\phi = 270°$ and $\phi = 90°$. Note that the blank area near the root is due to $-F'^*_x$ going to zero and the normalized error exceeding the colorbar limits, rather than being a region of zero error.

The cause for this band of overprediction is thought to be explained by Figure 4.11, which shows the component of kinematic velocity (i.e., velocity due to rotation and forward motion) in the spanwise direction[2] over a blade at a selection of azimuthal positions. Note the outward velocity at the blade tips in the downwind region; this crossflow is a result of the $V_{\infty,z}$ velocity component. In reality, outward crossflow at the tip would cause wake shedding off of the blade tip as if it were a trailing edge, but such shedding is not realized in RoBIN because wake shedding is prescribed only along the trailing edge. The lack of shedding at the tips is suspected to result in less downwash on and exaggerated lift from the adjacent blade sections. That the overprediction is a relatively constant percentage of $-F'_x$ at the tip supports the hypothesis of a wake-related inaccuracy because the strength

[2]The spanwise direction is not the same as the radial direction. The spanwise direction is normal to the blade root and tip edges and is the same across the entire blade for a given ϕ. In contrast, the radial direction points toward the propeller origin and would vary over a blade.

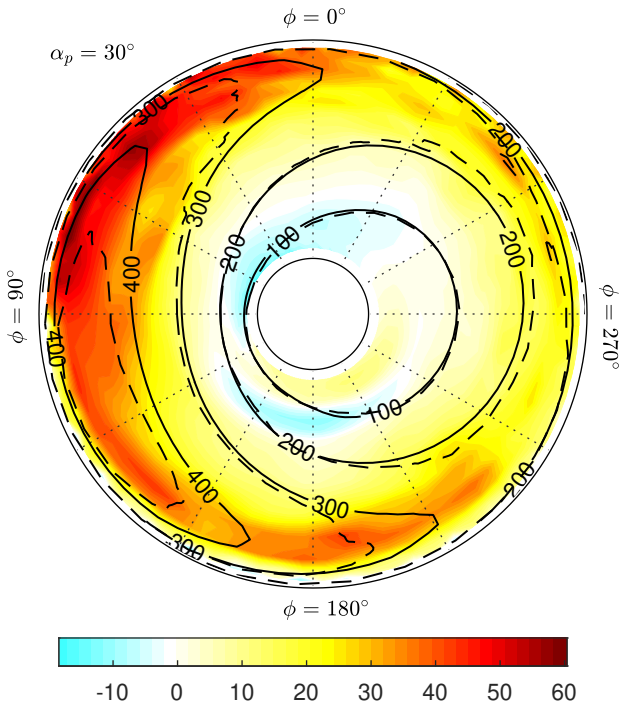

Figure 4.9: Contours of $-F'_x$ and $-F'^*_x$ at $\alpha_p = 30°$ overlaid on a colored map of the dimensional error. Solid contours are from RoBIN and dashed contours are from OVERFLOW.

of the wake shed, and therefore the strength of the downwash, is proportional to the lift. A similar tip-shedding effect should occur with the inward crossflow at the blade roots in the upwind region. However, $-F'^*_x$ is near zero here so it is difficult to assess whether the errors are due to modeling inaccuracy or divide-by-zero exaggeration.

Figure 4.12 shows a plot of F'_y, F'^*_y, and the dimensional error, $F'_y - F'^*_y$, and Figure 4.13 shows a similar plot of F'_z, F'^*_z, and $F'_z - F'^*_z$. In both instances, good agreement is found between the RoBIN and OVERFLOW contours with peak errors occuring in the root region, where the blade has the highest chord length. The peak errors for both forces are also consistent with a lack of viscous drag—in Figure 4.12, the leftward sweeping blade on the downwind side lacks a viscous drag force in the $-y$ direction, and in Figure 4.13, the downward sweeping blade on the advancing side lacks a viscous drag force in the $+z$ direction. Normalized error plots are not shown for F'_y and F'_z because there were widespread regions of near-zero F'^*_y and F'^*_z that made the plots ineffective.

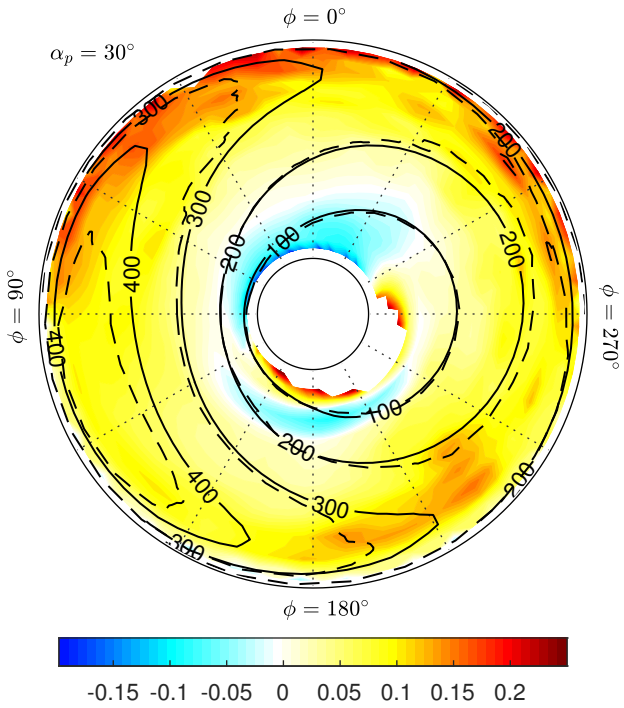

Figure 4.10: Contours of $-F'_x$ and $-F'^*_x$ at $\alpha_p = 30°$ overlaid on a colored map of the normalized error. Solid contours are from RoBIN and dashed contours are from OVERFLOW.

4.4.4 Angle of Attack Sweep for Propeller and Wing

For the propeller and wing case, the propeller geometry was discretized into 15 spanwise and chordwise panels per blade ($N_{ppb} = 225$), and the wing was discretized into 40 spanwise and chordwise panels. The time step size corresponded to $\Delta\phi = 7.2°$ ($N_{tpr} = 50$), and the cases were run until $N_{rev} = 8$. The range of α_p was reduced to $0° \leq \alpha_p \leq 30°$ because RoBIN is not capable of predicting the wing stall that occurs for $\alpha_p \gtrapprox 15°$.

Figure 4.14 shows the comparison of the propeller forces and moments with results from the isolated case included for reference. That OVERFLOW's $-F_x$ and M_x results are higher in the presence of the wing than in the isolated case is likely because of the blockage effect from the 18% thick wing. RoBIN's $-F_x$ and M_x results do not show this increase and are nearly identical to isolated results because the thin vortex lattice representation of the wing does not produce thickness effects. Good agreement is seen for M_y, which approximately doubles with the wing's presence. The overprediction at $\alpha_p = 0°$ is also

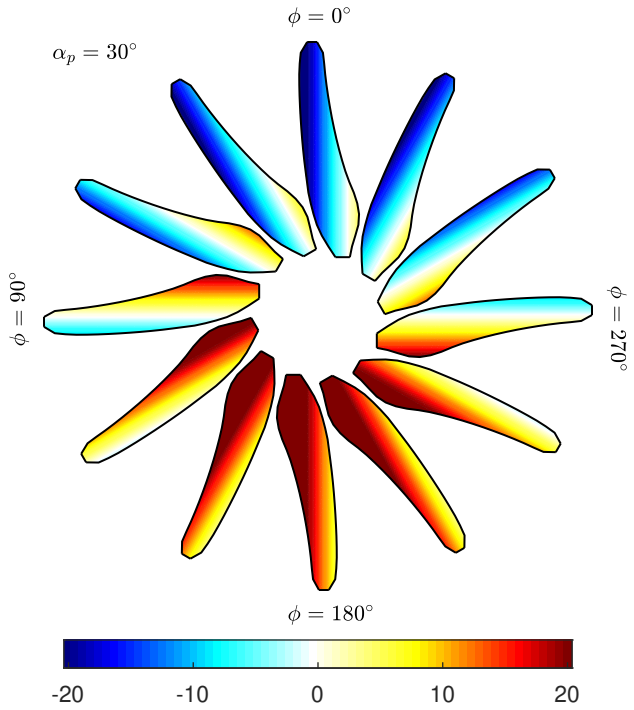

Figure 4.11: Shaded map of the component of kinematic velocity in the spanwise direction over a blade at various azimuthal positions. Positive values defined as inward toward the center.

attributed to the lack of blockage effects. Since the wing is positioned behind the upper (downwind) half of the propeller disk, the presence of blockage would increase thrust there and add a negative pitching moment that is not captured in RoBIN. As α_p increases, the wing blockage is projected further down the disk (toward the upwind side) so the negative pitching moment would decrease. The increases in F_z and M_z from isolated results indicate the presence of upwash from the wing, which increases the effective angle of attack observed by the propeller. The change in effective angle of attack can be estimated from the horizontal shift between the interacting and isolated results and is relatively consistent between F_z and M_z over the range of α_p. For example, both F_z and M_z at $\alpha_p = 10°$ in the presence of the wing are approximately equal to F_z and M_z at $\alpha_p = 15°$ in isolation.

Figure 4.15 shows the comparison of the wing forces and moments for completeness. The wing forces and moments were not expected to be as accurate as those of the propeller because the propeller wake passing through the wing allows many opportunities for exag-

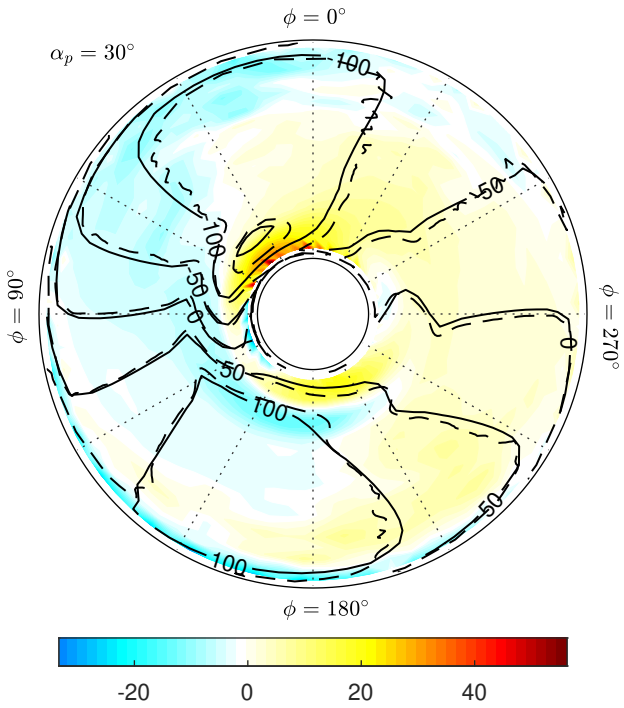

Figure 4.12: Contours of F'_y and F'^*_y at $\alpha_p = 30°$ overlaid on a colored map of the dimensional error. Solid contours are from RoBIN and dashed contours are from OVERFLOW.

gerated panel forces. If a wake vortex segment passes closely to a load calculation point on the wing, the vortex segment may induce an unrealistically high velocity (even with the vortex core model), leading to an exaggerated force from the respective bound segment. The inconsistency in the moment predictions, which are most sensitive to local peak loads, seem to reflect this problem. The lift and drag forces are less sensitive to local peak loads and trend closer with OVERFLOW results. The drag is understandably underpredicted due to a lack of viscous drag.

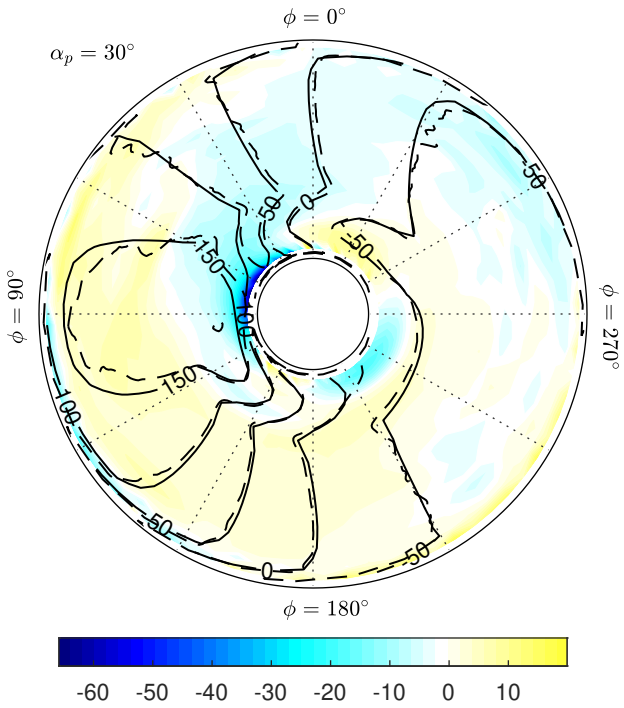

Figure 4.13: Contours of F'_z and F'^*_z at $\alpha_p = 30°$ overlaid on a colored map of the dimensional error. Solid contours are from RoBIN and dashed contours are from OVERFLOW.

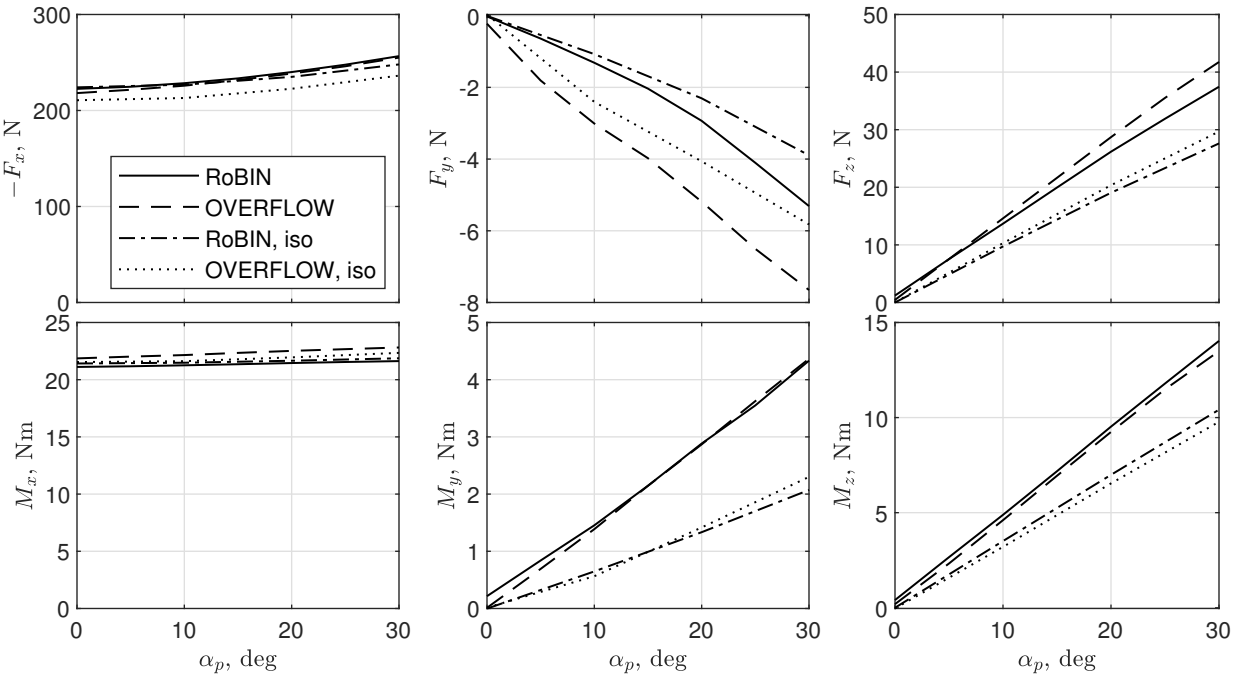

Figure 4.14: Comparison of RoBIN and OVERFLOW results for the propeller in the propeller and wing case over a sweep of α_p with isolated propeller results included.

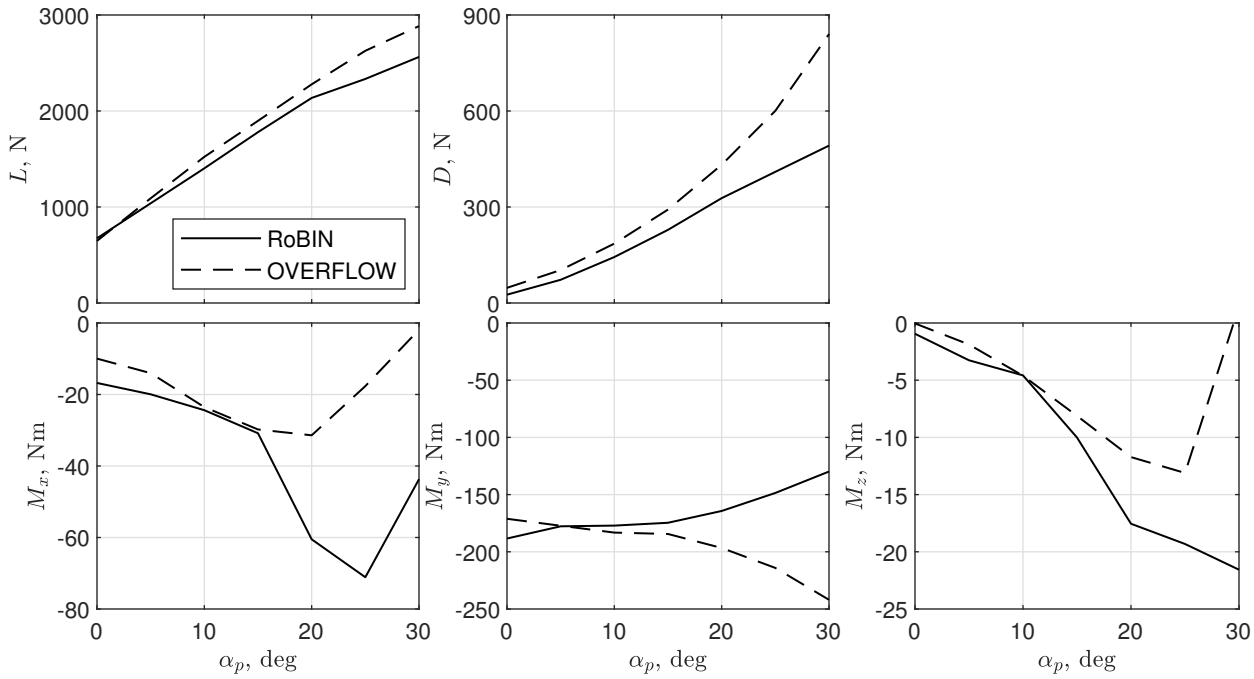

Figure 4.15: Comparison of RoBIN and OVERFLOW results for the wing in the propeller and wing case over a sweep of α_p.

4.5 Computation Time

Since the RoBIN and OVERFLOW results presented here were generated using different computing resources, we will avoid a rigorous comparison and only give an anecdotal account of the computation time. The RoBIN cases were run in sequence on a server with two Intel Xeon Platinum 8160 CPUs, but the Biot-Savart calculations were accelerated via four NVIDIA Tesla P4 GPUs. In the study of grid and time step resolution, the runtimes ranged from 20 seconds to 170 minutes per case. The resolution settings that were selected for the subsequent isolated propeller analyses (400 panels per blade and 72 time steps per revolution) required about 20 minutes per case. The OVERFLOW cases were run in parallel on the NASA Langley Research Center K3-subcluster using 16 Intel Xeon Processor E5-2670 CPUs for each case. The OVERFLOW cases all completed in about 60 hours.

CHAPTER 5
INVESTIGATING THE CAUSES OF PROPELLER PITCHING MOMENT

Although the X-57 HLP validation cases showed that propeller pitching moment could be modeled accurately, the relatively complicated geometry made it difficult to isolate the hypothesized induced velocity effects for testing. Thus, in this chapter, a set of simplified propeller and wing geometries are used to test the effects of a skewed wake and wing circulation on propeller pitching moment.

5.1 Geometry

The propeller geometry used is based on Leishman's ideally twisted rotor for hover [70], which is defined by a constant blade chord and the twist distribution,

$$\theta(r) = \frac{\theta_{tip}}{r/R} \tag{5.1}$$

where θ_{tip} is the blade twist at the tip. In reality, a VTOL propeller would most likely need a variable pitch mechanism to be efficient over the widely varying conditions between hover and forward flight. Thus, a collective pitch was added to Equation 5.1 to give

$$\theta(r) = \frac{\theta_{tip}}{r/R} + \theta_{coll} \tag{5.2}$$

For the following isolated propeller cases, $\theta_{tip} = 7°$, $\theta_{coll} = 5°$, and $R = 0.5$ m. The propeller has two blades of constant $0.15R$ chord that are constructed from flat plate airfoils stacked at the quarter-chord. No spinner was included but a hub cutout extending out to $0.2R$ was applied. The design operating condition was selected to be 3600 rpm at $V_\infty = 30$ m/s, which corresponds to an advance ratio of $J = 0.5$. For the propeller and wing cases, the same propeller was positioned in front of a rectangular 5 m span by 0.1 m chord wing

with flat plate airfoils. The wing was centered behind the propeller with the wing's quarter-chord $1R$ away from the propeller origin in the x direction and with the wing's chord plane (initially) parallel to the propeller's x-y plane.

The propeller blades were modeled with 20 spanwise panels each, the wing was modeled with 40 spanwise panels, and both the propeller blades and wing were modeled with a single row of chordwise panels. This single row of chordwise panels combined with the quarter-chord offset of the bound vortex rings from the physical geometry grid (as described in Section 3.1) meant that the leading edges of the bound vortex rings would be aligned along the surfaces' quarter chords, similar to a lifting line model. A simple lifting line-like model has two advantages here. First, since we are interested in the influence of induced velocities on blade forces, which are generated by only the leading edge segments of the bound vortex rings, we can probe the exact induced velocities along the single row of lifting vortex segments and avoid having to derive a chordwise average. Second, since wing circulation can be increased in several ways (chord, camber, angle of attack), a lifting line-like representation allows us to focus on the effect of changing circulation without having to worry about the variations in the distribution of vorticity associated with changes in wing geometry. Similar reasoning is behind the selection of a very short wing chord. The wing's circulation will be controlled by adjusting the wing inclination, and the short chord reduces the amount of variation in the wake-shedding location at the trailing edge. The propeller and wing, as modeled in RoBIN, are illustrated in Figure 5.1.

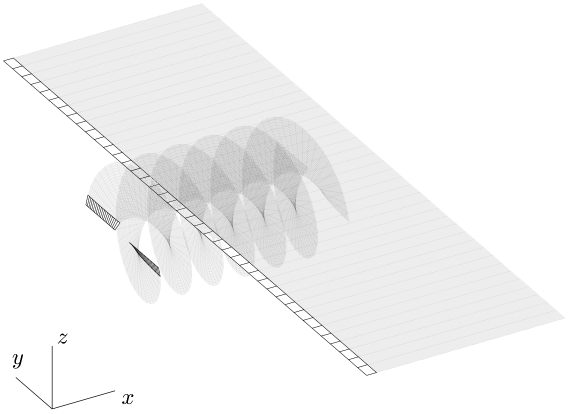

Figure 5.1: Generic propeller and wing as modeled in RoBIN visualized with a notional prescribed wake.

5.2 Testing the Effect of a Skewed Propeller Wake

To isolate the effect of a skewed wake on the propeller pitching moment of an isolated propeller, an ad hoc prescribed wake mode was added to RoBIN. The prescribed wake mode solved for the wake strength as usual but forced the wake to propagate as axisymmetric helices in the $+x$ direction at a velocity of $V_\infty cos(\alpha_p)$. This prescribed wake should, in effect, create an induced velocity distribution at the propeller disk that is asymmetric across the z axis (due to the advancing-retreating blade effect) but symmetric about the y axis, similar to the induced velocity distribution used by Ribner [13]. A sweep was conducted over $0^\circ < \alpha_p < 60^\circ$ and each simulation was run for eight revolutions with 72 time steps per revolution.

Figure 5.2 compares the propeller forces and moments resulting from the prescribed wake and free wake modes. The results show why early propeller induced velocity models that did not capture skewed-wake effects still tended to be useful; the prescribed wake predictions of $-F_x$, M_x, F_z, and M_z agree relatively well with those of the free wake, especially at lower α_p where conventional propellers would operate. However, the prescribed wake mode severely underpredicted M_y and F_y, which are nonzero only because the helical

wake geometry was not symmetric about the x-y plane.

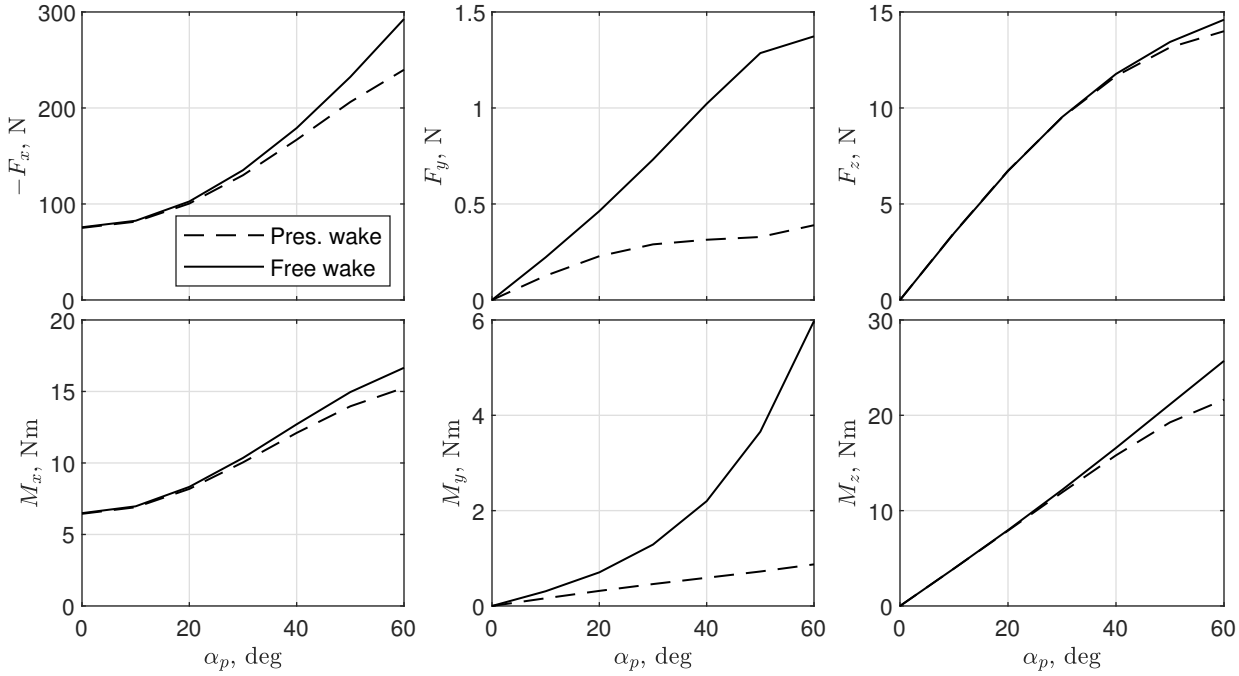

Figure 5.2: Comparison of propeller forces and moments over a sweep of α_p using prescribed wake and free wake modes.

For a more in-depth analysis, Figure 5.3 compares the x component of the total induced velocity (due to both bound and wake vortex rings) observed along the blades over the course of the last revolution from the prescribed and free wake modes at $\alpha_p = 30°$. The free wake mode resulted in lower induced velocities on the upwind half of the disk while the two modes produced nearly identical induced velocities on the downwind side. To better illustrate the difference, Figures 5.4 and 5.5 decompose the axial induced velocity into contributions from the bound and wake vortex rings, respectively. The bound contributions show relatively little difference whereas the wake contributions are clearly more negative on the upwind half of the disk in the free wake mode. Overall, these results suggest that the skewed wake effect is the primary cause of propeller pitching moment for an isolated propeller.

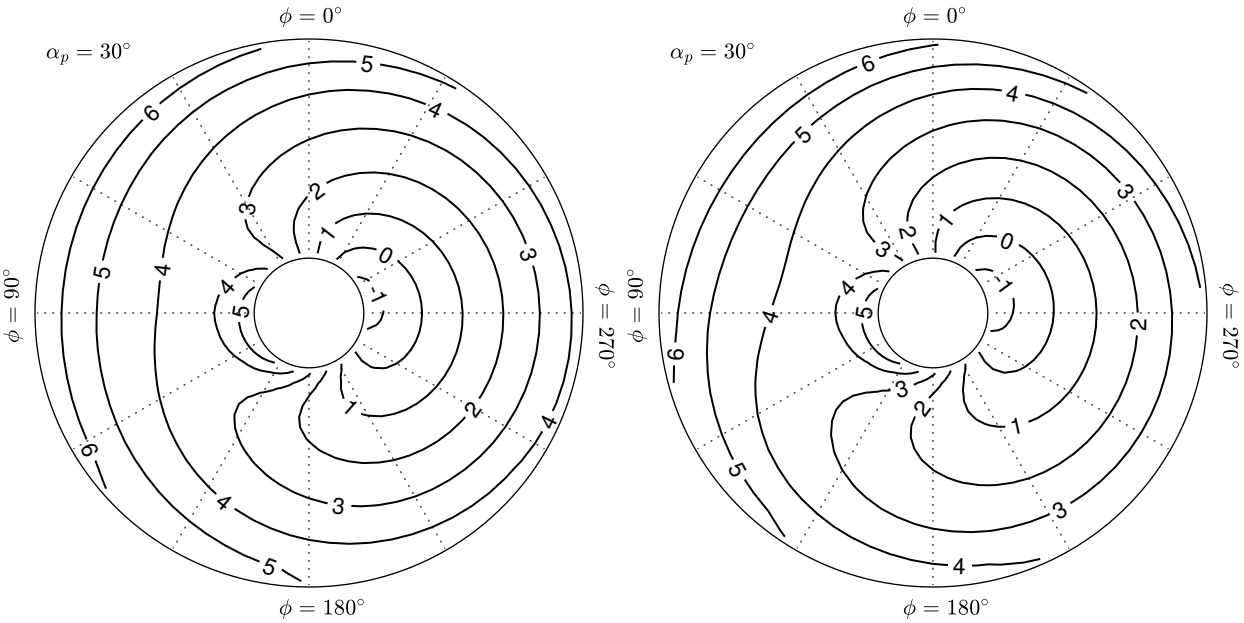

Figure 5.3: Contours of total axial induced velocity observed by the blades over the last revolution at $\alpha_p = 30°$. Prescribed wake mode (left) and free wake mode (right).

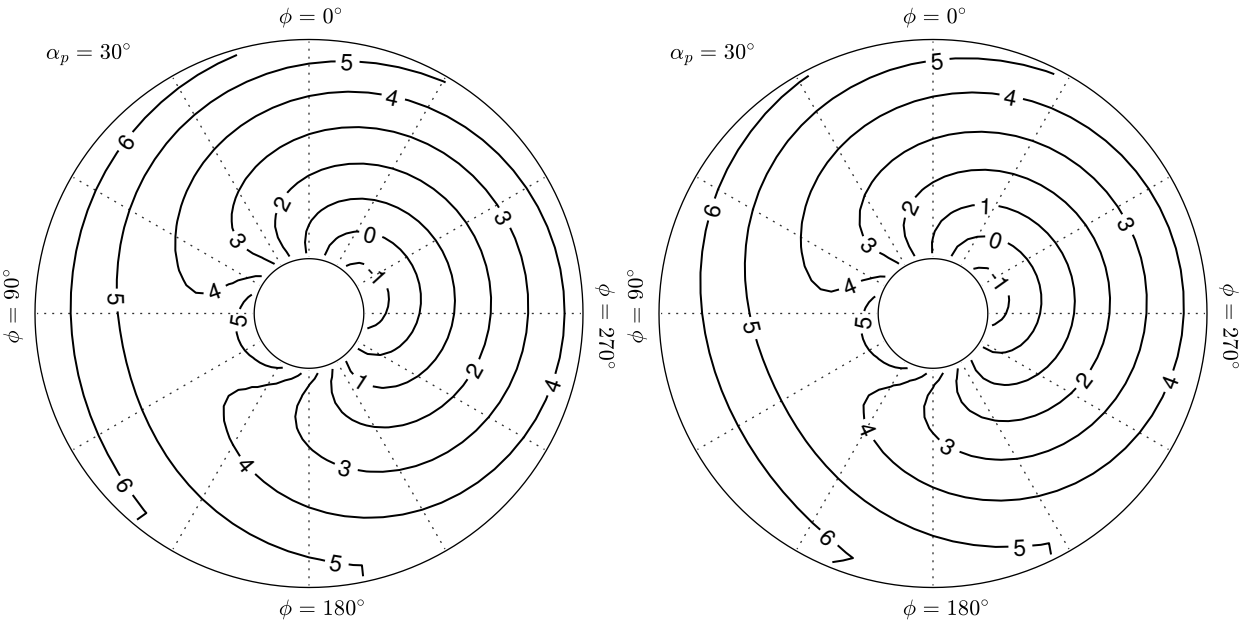

Figure 5.4: Contours of bound vortex rings' contribution to axial induced velocity observed by the blades at $\alpha_p = 30°$. Prescribed wake mode (left) and free wake mode (right).

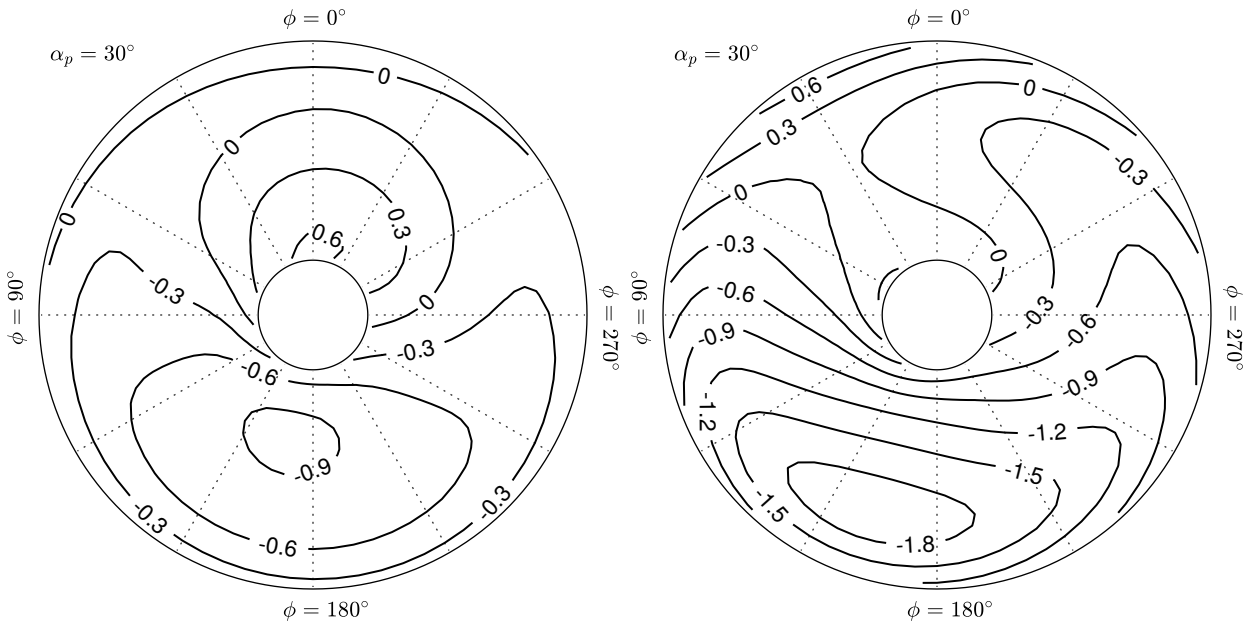

Figure 5.5: Contours of wake vortex rings' contribution to axial induced velocity observed by the blades at $\alpha_p = 30°$. Prescribed wake mode (left) and free wake mode (right).

5.3 Testing the Effect of Wing Circulation

To test the effect of wing circulation, the wing was independently inclined about its quarter-chord to $i_w = 0°, 10°$, and $20°$, which resulted in lift-to-thrust ratios of 0, 3.8, and 7.5, respectively, when $\alpha_p = 0°$. A sweep of $0° \leq \alpha_p \leq 30°$ was performed at each i_w with each simulation running for 10 revolutions at 40 time steps per revolution. Figure 5.6 shows the propeller forces and moments from these sweeps. Aside from the clear increases in F_y and M_y, increases in wing circulation have almost no effect on the other forces and moments. Only minute increases in F_z and M_z are observed, which is consistent with an increase in effective α_p induced by the wing's upwash.

Figure 5.7 shows the total axial induced velocity observed along the blades with the wing at $i_w = 0°$ and $20°$, respectively. The increase in i_w is seen to shift the contours upstream such that the upstream half of the disk experiences less downwash than the downwind half, consistent with the increase in pitching moment seen in Figure 5.6. Figures 5.8

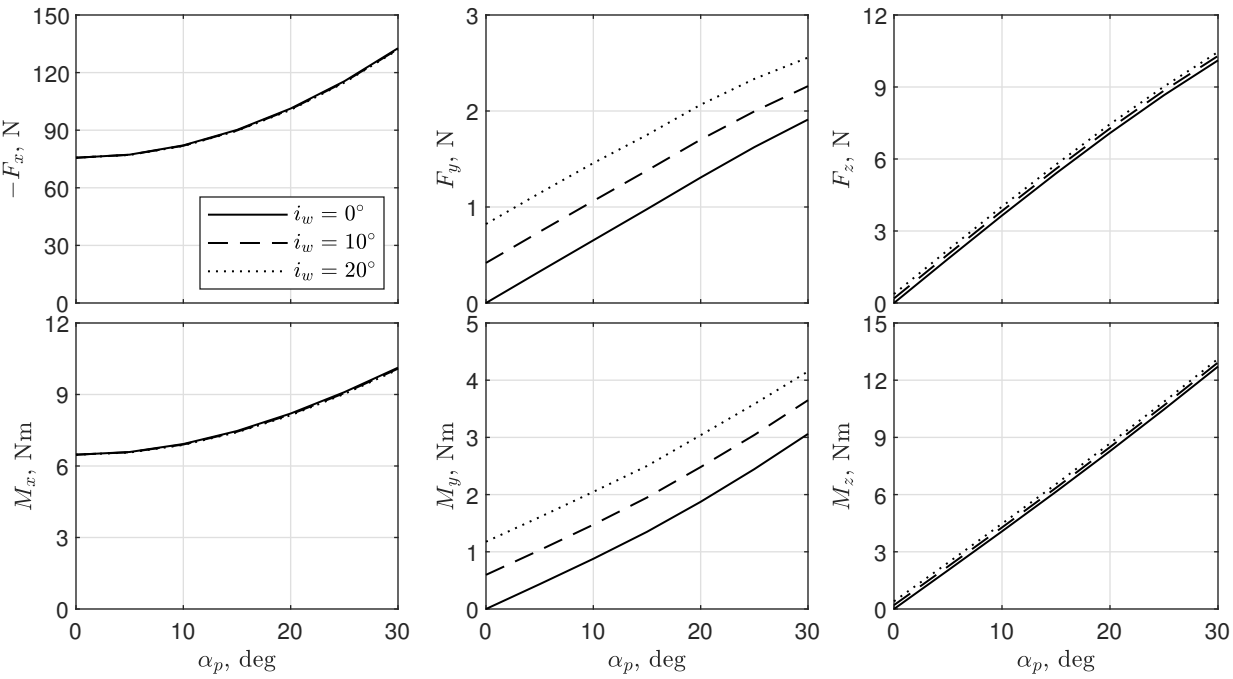

Figure 5.6: Comparison of propeller forces and moments over a sweep of α_p with varying α_w.

and 5.9 shows the decomposition of the axial induced velocity into contributions from the propeller (and its wake) and the wing (and its wake), respectively. Compared to the propeller's self-induced axial velocity, which is actually slightly less on the downwind side, the wing's contributions are more positive on the downwind side and are clearly responsible for the increase in pitching moment observed in Figure 5.6. To summarize, it is not the wing's upwash, but rather the "forewash" and "aftwash" that causes an asymmetric axial induced velocity distribution across the propeller disk, resulting in a propeller pitching moment.

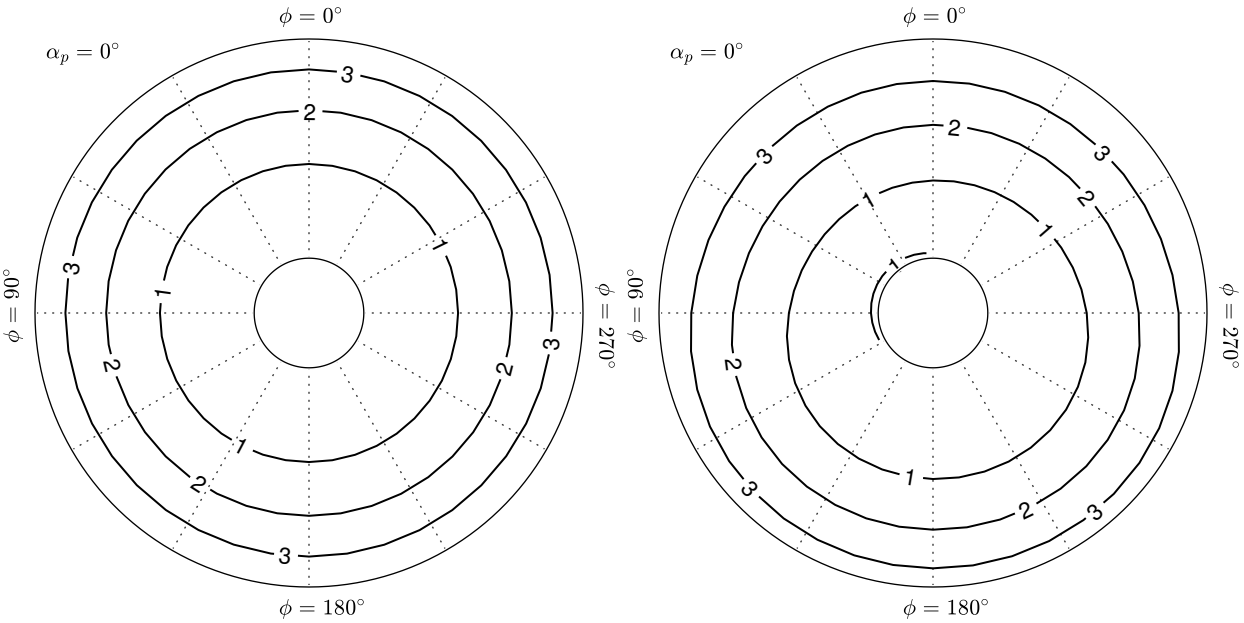

Figure 5.7: Contours of total axial induced velocity observed by the blades over the last revolution at $\alpha_p = 0°$. $i_w = 0°$ (left) and $i_w = 20°$ (right).

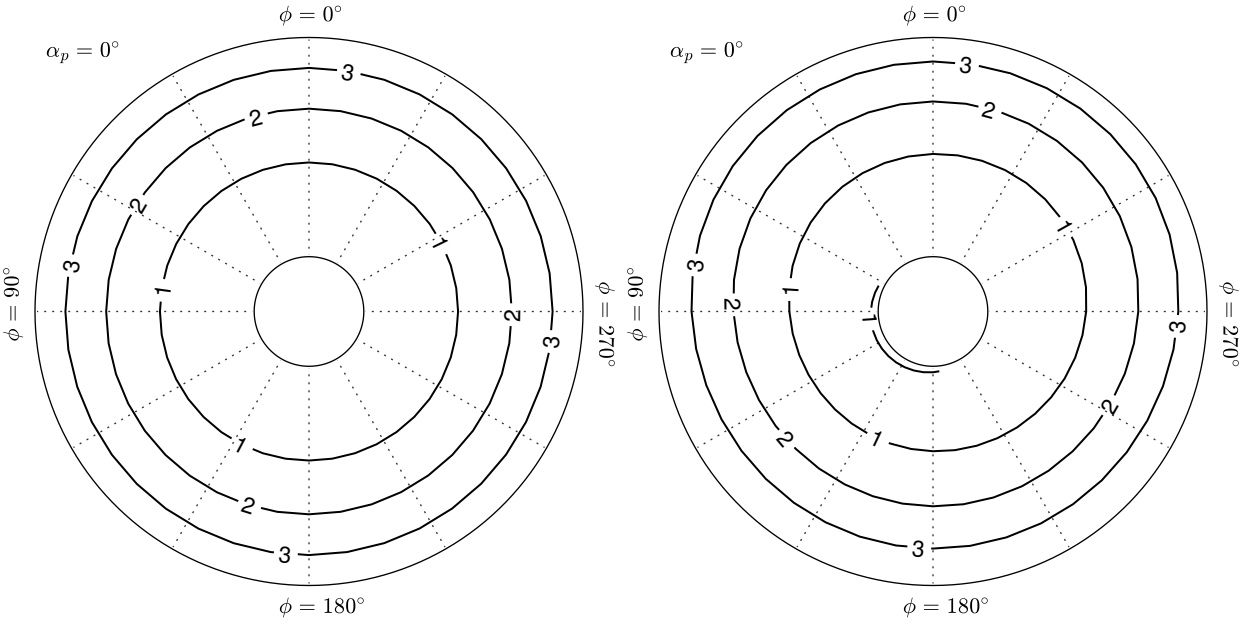

Figure 5.8: Contours of the propeller's bound and wake vortex rings' contribution to axial induced velocity observed by the blades at $\alpha_p = 0°$. $i_w = 0°$ (left) and $i_w = 20°$ (right).

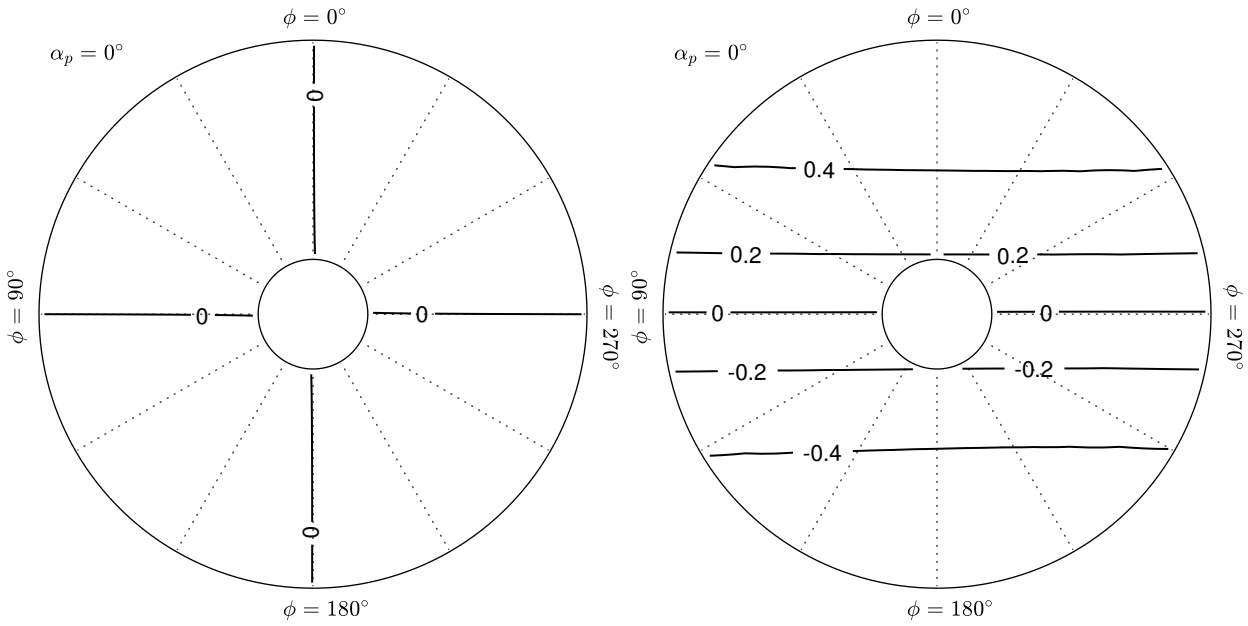

Figure 5.9: Contours of the wing's bound and wake vortex rings' contribution to axial induced velocity observed by the blades at $\alpha_p = 0^\circ$. $i_w = 0^\circ$ (left) and $i_w = 20^\circ$ (right).

CHAPTER 6
INVESTIGATING THE CONDITIONS FOR SIGNIFICANCE

It is evident from aviation history that propeller pitching moment was not a defining constraint in the stability and control of conventional takeoff and landing aircraft. The relatively low angles of attack and high flight speeds of CTOL aircraft would result in insignificant magnitudes of propeller pitching moment relative to the aircraft's control authority. However, observations from previous VTOL aircraft suggest that the low flight speeds and high angles of attack encountered by propellers during transition invalidate the assumptions of insignificance.

In this chapter, we use RoBIN to explore the conditions under which propeller pitching moment becomes significant for aircraft. First, we explore the characteristic trends of propeller pitching moment by generating performance maps over ranges of transition operational parameters. Then, we derive a generalizable metric of significance using the generated maps and a series of justifiable simplifying assumptions. The studies will be limited to isolated propellers because the inviscid nature of RoBIN's analysis precludes accurate solutions of propeller and wing configurations at high angles of attack where the wing is fully stalled. However, given the revelations from the previous chapters on the effect of wing circulation, these results will still serve a useful purpose as a conservative lower bound for aircraft that have (upstream) propeller-wing interaction.

6.1 Pitching Moment Trends during Transition

Instead of using dimensional metrics, as has been the case thus far, the results presented here are in terms of nondimensional coefficients so that they may be generalized to propellers and aircraft of varying scale. Two types of coefficients are used: the "plain" coefficients (e.g., C_{Fx}) are normalized by tip dynamic pressure, whereas the coefficients with an

infinity superscript (e.g., C_{Fx}^{∞}) are normalized by freestream dynamic pressure. The general forms of the force and moment coefficients are

$$C_F = \frac{F}{\rho_\infty n^2 {D_p}^4} \tag{6.1}$$

$$C_M = \frac{M}{\rho_\infty n^2 {D_p}^5} \tag{6.2}$$

$$C_F^\infty = \frac{F}{\frac{1}{2}\rho_\infty V_\infty^2 A_p} \tag{6.3}$$

$$C_M^\infty = \frac{M}{\frac{1}{2}\rho_\infty V_\infty^2 A_p D_p} \tag{6.4}$$

where n is the rotation speed in rev/s, A_p is the propeller area, and D_p is the propeller diameter. A useful property of these nondimensional coefficients is that, in the context of inviscid analysis, they are constant for a given propeller geometry at a given advance ratio and angle of attack, regardless of dimensional rotation speed, freestream velocity, or diameter via geometric scaling. Appendix A demonstrates this property.

Figure 6.1 shows a map of C_{My} divided by $-C_{Fx}$ over J and α_p. $C_{My}/-C_{Fx}$ reduces down to $M_y/(-F_x \times D_p)$, which is the percentage of the diameter by which the thrust vector must be translated down from the rotation axis to produce a moment about the origin equal to the propeller pitching moment. The sharp rise in $C_{My}/-C_{Fx}$ in the $\alpha_p = 0^\circ$ and $J = 0.6$ corner is where the propeller rotates too slowly and thrust coefficient goes to zero in the denominator. At $J < 0.3$, $C_{My}/-C_{Fx}$ generally tends to increase with J due to the wake becoming more skewed away from the rotation axis. Since the skewed wake causes the induced velocity asymmetry over the propeller disk, larger skew angles result in larger pitching moments. However, $C_{My}/-C_{Fx}$ does not necessarily continue to increase with J. At higher α_p where the propeller maintains positive thrust at $J > 0.3$, $C_{My}/-C_{Fx}$ is seen to decrease as J increases. This is because the wake skew is limited by and asymptotes toward the freestream direction, and the diminishing increases in skew is counteracted by

the wake stretching further over a single revolution at higher J. Since vortex velocity influence has an inverse-squared relationship with distance, the difference in the velocity influence magnitude at any two points on the propeller disk diminishes as the influencing vortex becomes further removed. Figure 6.2 visualizes the wakes of several $\alpha_p = 90°$ propellers at varying J to demonstrate the stretching and asymptotic skewing of the wake.

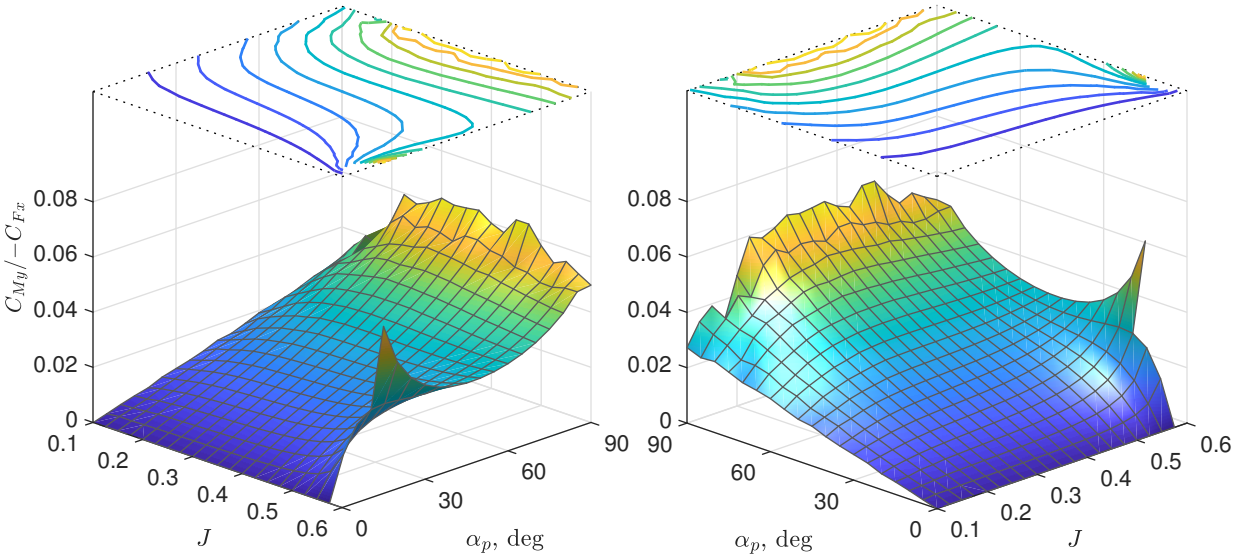

Figure 6.1: Surface of $C_{My}/-C_{Fx}$ over advance ratio and angle of attack.

Although $C_{My}/-C_{Fx}$ is useful for understanding how propeller pitching moment trends with different operating conditions, it is not necessarily representative of the propeller pitching moment's significance to aircraft. Many modern VTOL aircraft concepts can achieve trim via passive control surfaces or via differential thrust over distributed propulsors. If the propeller pitching moment were to be trimmed by an unblown horizontal stabilizer, whose control authority would be proportional to the freestream dynamic pressure, C_{My}^{∞} would be the appropriate metric for comparison. Figure 6.3 shows the surface of C_{My}^{∞} over J and α_p, where C_{My}^{∞} rises rapidly as J decreases and α_p increases. The trend would likely continue to an extent as J decreased further, though it is unclear whether C_{My}^{∞} would ultimately resolve at zero or infinity at the indeterminate condition of $J = 0$. Figure 6.3 also provides more evidence as to why propeller pitching moment had not received much

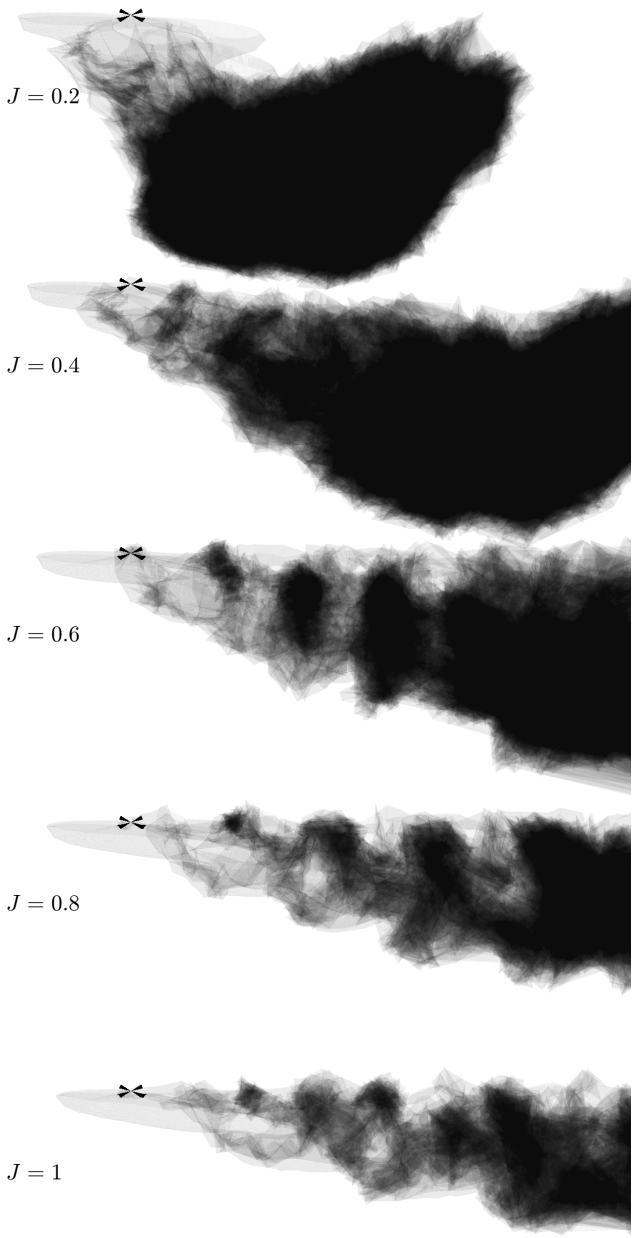

Figure 6.2: Wake visualization at a selection of advance ratios. $\alpha_p = 90°$, $N_{rev} = 8$, freestream direction left to right.

attention in the literature; C^{∞}_{My} is very low in the $\alpha_p \leq 20°$ region where propellers on conventional aircraft typically operate.

If, instead, the pitching moment were to be trimmed by differential thrust (via another identical propeller), then the appropriate metric would be similar to $C_{My}/-C_{Fx}$, shown

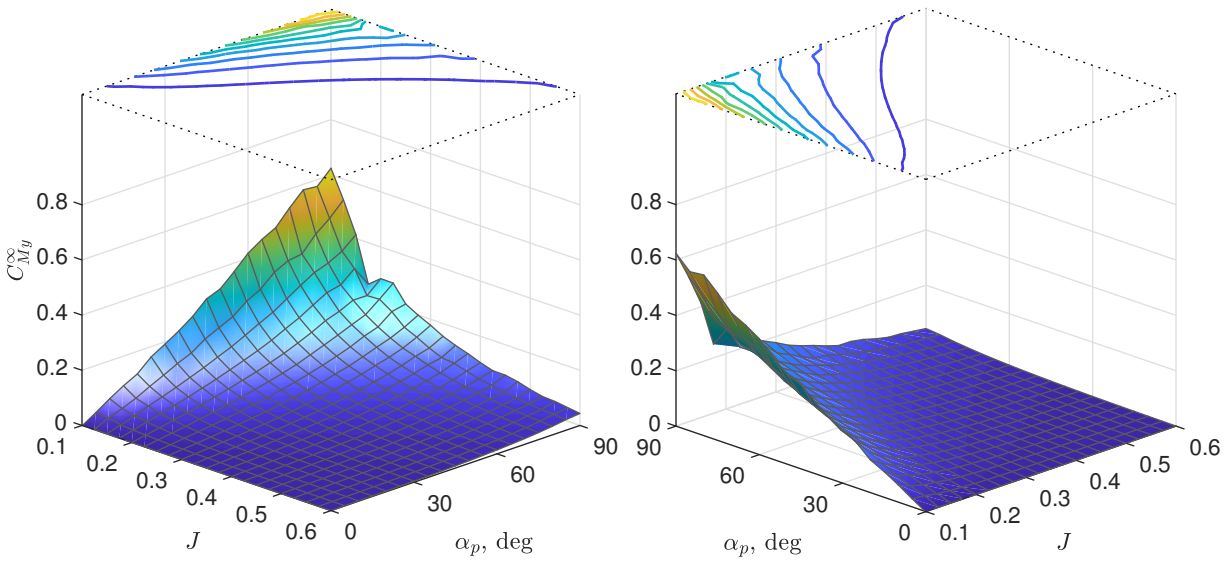

Figure 6.3: Surface of C_{My}^{∞} over advance ratio and angle of attack.

in Figure 6.1, except with the D_p reference length in the denominator replaced by the moment arm of the trimming propeller relative to the aircraft center of gravity. Unlike C_{My}^{∞}, the $C_{My}/-C_{Fx}$ surface does not peak at near-zero J because the control authority of a propeller does not go to zero at static conditions.

6.2 A Generalizable Metric for Significance

To provide generalizable insight into the significance of propeller pitching moment, the following section describes the development of a metric that expresses propeller pitching moment as an effective displacement of the center of gravity in percent chord of the main wing.

Consider a tiltrotor-like VTOL aircraft with N_p identical propellers of area A_p that tilt through a range of α_p to transition between hover and cruise. In hover, it is assumed that the entire aircraft's weight, W, is distributed evenly amongst the propellers such that the disk loading in hover is $p_{DL} = \frac{W}{N_p A_p}$. Similarly, in cruise, it is assumed that W is fully supported by the lift of a main wing of area S_w so that the wing loading in cruise is $p_{WL} = \frac{W}{S_w}$. For simplicity, the propellers' thrust, $-F_x = -C_{Fx}^{\infty} q_{\infty} A_p$, is assumed to be the only propeller

force, and the main wing's lift, $L = C_L q_\infty S_w$, at any point is assumed to be generated at a constant lift coefficient. Lastly, we assume a rectangular wing with with aspect ratio $\mathcal{AR}$ so that the final expression can be represented in units of percent chord.

Given values of N_p, p_{DL}, p_{WL}, C_L, and $\mathcal{AR}$, start by satisfying the vertical force balance for a level transition,

$$W = -C_{Fx}^{\infty} q_\infty A_p N_p \sin\alpha_p + C_L q_\infty S_w \tag{6.5}$$

Solving for the $-C_{Fx}^{\infty}$ required at a specific q_∞ and α_p gives

$$-C_{Fx}^{\infty} = \frac{W - C_L q_\infty S_w}{q_\infty N_p A_p \sin\alpha_p} = \frac{p_{DL} - \dfrac{C_L q_\infty p_{DL}}{p_{WL}}}{q_\infty \sin\alpha_p} \tag{6.6}$$

Then, use the data in Figure 6.4 to interpolate for the J that satisfies $-C_{Fx}^{\infty}$ at the specified α_p.

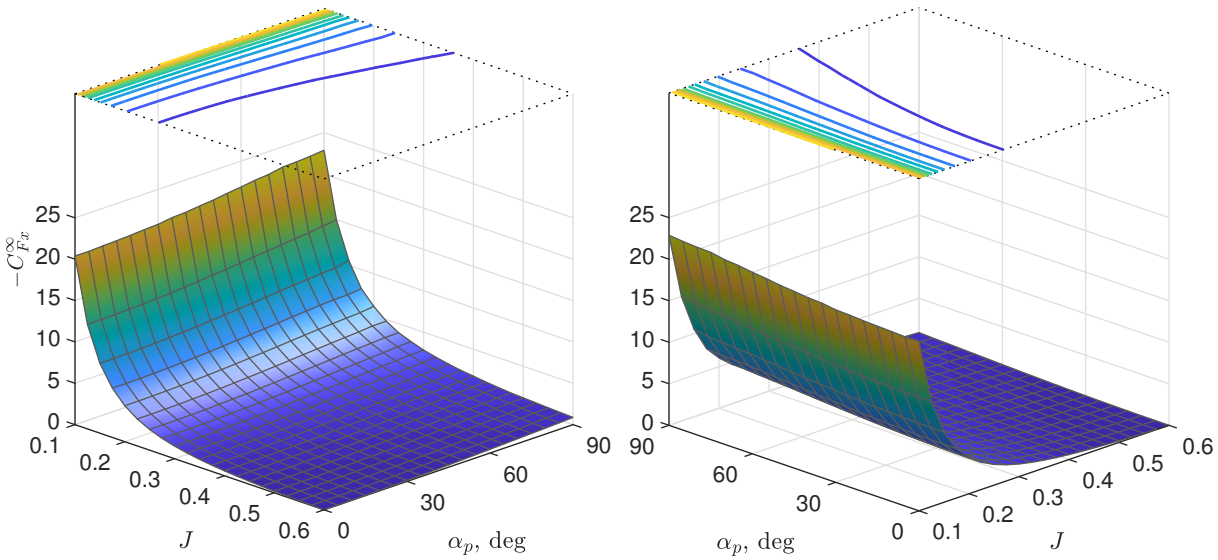

Figure 6.4: Surface of $-C_{Fx}^{\infty}$ over advance ratio and angle of attack.

The interpolated J and α_p are then referenced using the data in Figure 6.3 to find the C_{My}^{∞}

that would be produced by each propeller. Since

$$C_{My}^{\infty} = \frac{M_y}{q_{\infty} A_p D_p} \tag{6.7}$$

solve for M_y and express D_p in terms of A_p,

$$M_y = C_{My}^{\infty} q_{\infty} A_p 2\sqrt{A_p/\pi} \tag{6.8}$$

Lastly, multiply both sides by N_p/Wc and manipulate the right-hand side into expressions of known values to get

$$\frac{N_p M_y}{Wc} = \frac{2C_{My}^{\infty} q_{\infty} \sqrt{A_p/\pi}}{p_{DL} c} = 2C_{My}^{\infty} q_{\infty} \sqrt{\frac{\mathit{A\!R} p_{WL}}{\pi N_p {p_{DL}}^3}} \tag{6.9}$$

The metric $\frac{N_p M_y}{Wc}$ is the total propeller pitching moment expressed in units of aircraft weight times wing chord, and because propeller-wing interaction was ignored, the metric as presented would be a conservative estimate in most cases. To demonstrate, Figure 6.5 shows the surface of $\frac{N_p M_y}{Wc}$ for an aircraft that uses the generic propeller with $N_p = 6$, $p_{DL} = 5$ lb/ft^2, $p_{WL} = 15$ lb/ft^2, $C_L = 0.65$, and $\mathit{A\!R} = 5$. The peak of roughly 0.1 means that the aircraft center of gravity is effectively shifted ten percent chord aft compared to if the propellers' thrust vectors were assumed to be centered at their hubs. However, an actual transition profile for a tiltrotor is unlikely to pass through the point $\alpha_p = 90°, V_{\infty} = 40$ m/s, and a more realistic peak would be around eight percent for this aircraft.

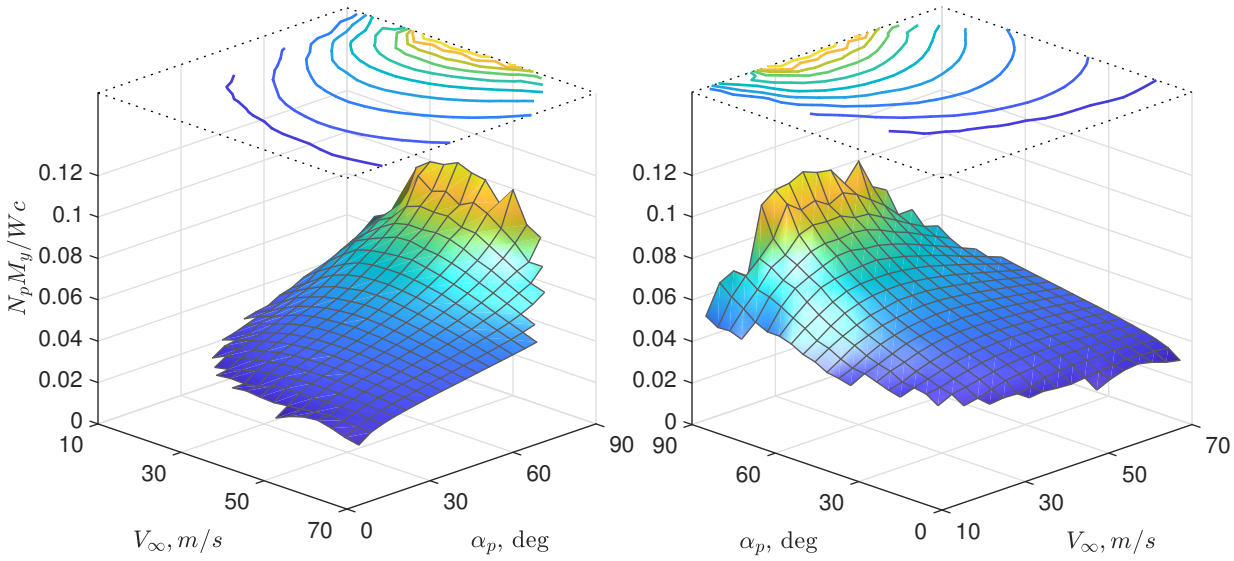

Figure 6.5: Example surface of N_pM_y/Wc over freestream velocity and angle of attack.

CHAPTER 7
CONCLUSION

In this dissertation, we have shown that propellers operating at an angle of attack experience a pitching moment about their hub that is primarily caused by an asymmetry in the axial induced velocity distribution over the disk about the pitch axis. The effect is present for isolated propellers, but interactions with other components can further increase the pitching moment. In the case of an isolated propeller, the wake skews in the freestream direction, resulting in reduced induced velocity on and increased thrust from the upwind half of the propeller. In the case of a propeller positioned upstream of a lifting wing, the wing's circulation similarly reduces the induced velocity on the upwind half while also increasing the induced velocity on the downwind half of the propeller.

Compared to the shaft torque and yawing moment, propeller pitching moment is the weakest of the propeller moments. However, the magnitudes are still considerable at low advance ratios and high angles of attack where VTOL aircraft must operate to transition between hover and forward flight. A conservative estimate using generic geometries puts the peak total propeller pitching moment on the order of an effective displacement of the aircraft center of gravity by several percent of the wing chord. Furthermore, the pitching moment is destabilizing in nature and, unlike the yawing moment, cannot be counteracted by a symmetrical placement of propellers about the aircraft.

Since the most significant pitching moments occur at low freestream velocities, passive stabilizers that depend on airspeed for control authority are not a feasible solution for stability and control in transition. During the previous VTOL era, later aircraft designs converged toward a hybrid tiltwing-deflected slipstream approach whereby a large-chord flap was integrated on a blown tilting wing [71, 72, 73, 74]. The flap, which generated a large negative pitching moment, would be programmed with a deflection schedule through-

out transition to counteract the positive propeller pitching moment. Vehicles such as the Canadair CL-84 [75] and retrofitted VZ-2 [76] demonstrated this approach. Fortunately, with the advent of distributed electric propulsion, modern VTOLs should not be severely inconvenienced by the requirement of an active trim mechanism.

Ultimately, we believe that propeller pitching moment is not a particularly crippling effect for VTOL aircraft. However, the nuanced physics and lack of understanding in the community are likely to lead to its omittance from consideration during conceptual design. We hope that the insights given here will help designers realize the importance of propeller pitching moment earlier and avoid costly changes later in their design process.

Appendices

APPENDIX A

CONSTANCY OF AERODYNAMIC COEFFICIENTS WITH ADVANCE RATIO

In the context of an inviscid solution, aerodynamic coefficients are constant for a given advance ratio regardless of the dimensional freestream velocity, rotation speed, and propeller diameter. Figures A.1 and A.2 show the thrust and pitching moment coefficients, respectively, of a generic propeller operated at $\alpha_p = 60^\circ$ over a range of advance ratios. Each plot contains nine curves for each coefficient, with each curve representing the same advance ratio sweep achieved by appropriately varying the rotation speed for three different freestream velocities and with the propeller geometrically scaled to three different diameters. The curves are largely identical with the measurements fanning out gradually at the lower advance ratios. The fanning out is due to the chaotic nature of the wake propagation in high loading conditions; slight differences in velocity influence due to numerical imprecision propagate over time, resulting in wake structure differences significant enough to affect the induced velocity distribution at the disk. The coefficient variations seem to be random in nature, inferred by the intersection of curves between different advance ratios, and can be considered noise in the data. The noise is more pronounced in the pitching moment coefficients than the thrust coefficients because the wake structure discrepancies primarily affect the *distribution* of induced velocity at the disk rather than the average. Based on this study, we limited the range of advance ratios examined to $J \geq 0.1$.

The simulation settings used were $N_{ppb} = 225$, $N_{tpr} = 60$, and $N_{rev} = 8$. If computation time were not an issue, the wake propagation noise could be reduced by increasing either the grid or timestep resolutions.

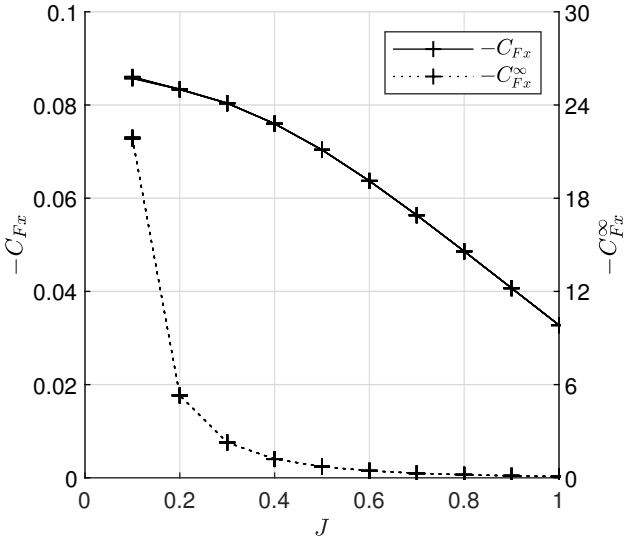

Figure A.1: Study over advance ratio.

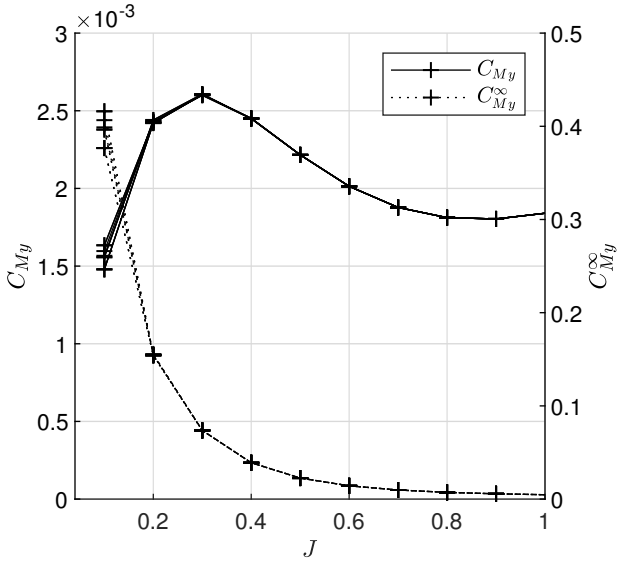

Figure A.2: Force coefficients versus advance ratio for generic propeller at $\alpha_p = 60°$.

REFERENCES

[1] J. P. Reeder, "Handling qualities experience with several vtol research aircraft," in *NASA Conference on V/STOL Aircraft*, 1960.

[2] W. A. Newsom Jr and L. P. Tosti, "Force-test investigation of the stability and control characteristics of a 1/4-scale model of a tilt-wing vertical-take-off-and-landing aircraft," National Aeronautics and Space Administration, Tech. Rep. NASA-MEMO-11-3-58L, 1959.

[3] L. P. Tosti, "Flight investigation of the stability and control characteristics of a 1/4-scale model of a tilt-wing vertical-take-off-and-landing aircraft," National Aeronautics and Space Administration, Tech. Rep. NASA-MEMO-11-4-58L, 1959.

[4] ——, "Aerodynamic characteristics of a 1/4-scale model of a tilt-wing vtol aircraft at high angles of wing incidence," National Aeronautics and Space Administration, Tech. Rep. NASA-TN-D-390, 1960.

[5] ——, "Longitudinal stability and control of a tilt-wing vtol aircraft model with rigid and flapping propeller blades," National Aeronautics and Space Administration, Tech. Rep. NASA-TN-D-1365, 1962.

[6] R. J. Pegg, "Summary of flight-test results of the vz-2 tilt-wing aircraft," National Aeronautics and Space Administration, Tech. Rep. NASA-TN-D-989, 1962.

[7] M. P. Fink, "Full-scale wind-tunnel investigation of the vz-5 four-propeller deflected-slipstream vtol airplane," National Aeronautics and Space Administration, Tech. Rep. NASA-TM-SX-805, 1963.

[8] H. A. James, R. C. Wingrove, C. A. Holzhauser, and F. J. Drinkwater III, "Wind-tunnel and piloted flight simulator investigation of a deflected-slipstream vtol airplane, the ryan vz-3ry," National Aeronautics and Space Administration, Tech. Rep. NASA-TN-D-89, 1959.

[9] H. L. Turner and F. J. Drinkwater III, "Longitudinal trim characteristics of a deflected slipstream v/stol aircraft during level flight at transition flight speeds," National Aeronautics and Space Administration, Tech. Rep. NASA-TN-D-1430, 1962.

[10] ——, "Some flight characteristics of a deflected slipstream v/stol aircraft," National Aeronautics and Space Administration, Tech. Rep. NASA-TN-D-1891, 1963.

[11] J. W. Draper and R. E. Kuhn, "Investigation of the aerodynamic characteristics of a model wing-propeller combination and of the wing and propeller separately at

angles of attack up to 90 degrees," National Advisory Committee for Aeronautics, Tech. Rep. NACA-TN-3304, 1954.

[12] R. E. Kuhn and J. W. Draper, "An investigation of a wing-propeller configuration employing large-chord plain flaps and large-diameter propellers for low-speed flight and vertical take-off," National Advisory Committee for Aeronautics, Tech. Rep. NASA-TN-3307, 1954.

[13] H. S. Ribner, "Propellers in yaw," National Advisory Committee for Aeronautics, Tech. Rep. NACA-TR-820, 1945.

[14] W. F. Phillips, E. A. Anderson, and Q. J. Kelly, "Predicting the contribution of running propellers to aircraft stability derivatives," *Journal of Aircraft*, vol. 40, no. 6, pp. 1107–1114, 2003.

[15] J. De Young, "Propeller at high incidence," *Journal of Aircraft*, vol. 2, no. 3, pp. 241–250, 1965.

[16] O. Flachsbart and G. Krober, "Experimental investigation of aircraft propellers exposed to oblique air currents," National Advisory Committee for Aeronautics, Tech. Rep. NACA-TM-562, 1930.

[17] E. P. Lesley, G. F. Worley, and S. Moy, "Air propellers in yaw," National Advisory Committee for Aeronautics, Tech. Rep. NACA-TR-597, 1937.

[18] R. E. Pendley, "Effect of propeller-axis angle of attack on thrust distribution over the propeller disk in relation to wake-survey measurement of thrust," National Advisory Committee for Aeronautics, Tech. Rep. NACA-ARR-L5J02b, 1945.

[19] H. C. McLemore and M. D. Cannon, "Aerodynamic investigation of a four-blade propeller operating through an angle-of-attack range from 0 to 180 degrees," National Advisory Committee for Aeronautics, Tech. Rep. NACA-TN-3228, 1954.

[20] P. F. Yaggy and V. L. Rogallo, "A wind-tunnel investigation of three propellers through an angle-of-attack range from 0 to 85 degrees," National Aeronautics and Space Administration, Tech. Rep. NASA-TN-D-318, 1960.

[21] P. L. Coe Jr, G. L. Gentry Jr, and D. M. Dunham, "Low-speed wind-tunnel tests of an advanced eight-bladed propeller," National Aeronautics and Space Administration, Tech. Rep. NASA-TM-86364, 1985.

[22] W. H. Reed III and S. R. Bland, "An analytical treatment of aircraft propeller precession instability," National Aeronautics and Space Administration, Tech. Rep. NASA-TN-D-659, 1961.

[23] J. C. Houbolt and I. Wilmer H. Reed, "Propeller-nacelle whirl flutter," *Journal of the Aerospace Sciences*, vol. 29, no. 3, pp. 333–346, 1962.

[24] S. R. Bland and R. M. Bennett, "Wind-tunnel measurement of propeller whirl-flutter speeds and static-stability derivatives and comparison with theory," National Aeronautics and Space Administration, Tech. Rep. NASA-TN-D-1807, 1963.

[25] H. Fluk, "The x-19 v/stol technology: A critical review," Air Force Flight Dynamics Laboratory, Tech. Rep. AFFDL-TR-66-195, 1967.

[26] Y. Leng, H. Yoo, T. Jardin, M. Bronz, and J.-M. Moschetta, "Aerodynamic modeling of propeller forces and moments at high angle of incidence," in *AIAA Scitech 2019 Forum*, AIAA 2019-1332, 2019.

[27] B. Theys, G. Dimitriadis, P. Hendrick, and J. De Schutter, "Experimental and numerical study of micro-aerial-vehicle propeller performance in oblique flow," *Journal of Aircraft*, vol. 54, no. 3, pp. 1076–1084, 2017.

[28] M. Misiorowski, F. Gandhi, and P. Anusonti-Inthra, "Computational analysis of rotor-blown-wing for evtol applications," in *Vertical Flight Society 75th Annual Forum and Technology Display*, 2019.

[29] J. G. Schepers, "Engineering models in wind energy aerodynamics: Development, implementation and analysis using dedicated aerodynamic measurements," Ph.D. dissertation, TU Delft, 2012.

[30] R. Niemiec and F. Gandhi, "Effects of inflow model on simulated aeromechanics of a quadrotor helicopter," in *72nd Annual Forum of the American Helicopter Society International*, 2016.

[31] M. Misiorowski, F. Gandhi, and A. A. Oberai, "Computational study on rotor interactional effects for a quadcopter in edgewise flight," *AIAA Journal*, vol. 57, no. 12, pp. 5309–5319, 2019.

[32] *Helicopter Flying Handbook*. United States Department of Transportation, Federal Aviation Administration, Airman Testing Branch, 2019, FAA-H-8083-21B.

[33] S. Gudmundsson, *General Aviation Aircraft Design: Applied Methods and Procedures*. Butterworth-Heinemann, 2013.

[34] W. Amatt, W. E. Bates, and H. V. Borst, "Summary of propeller design procedures and data. volume 2. structural analysis and blade design," US Army Air Mobility Research and Development Laboratory, Tech. Rep. AD-774-836, 1973.

[35] M. L. Masquelier, "Application of the vortex-lattice method to propeller performance analysis," M.S. thesis, Air Force Institute of Technology, 1982.

[36] M. Kobayakawa and H. Onuma, "Propeller aerodynamic performance by vortex-lattice method," *Journal of Aircraft*, vol. 22, no. 8, pp. 649–654, 1985.

[37] R. Van Houten, "Analysis of ducted propellers in steady flow," Naval Sea Systems Command, Tech. Rep. AD-A170-384, 1986.

[38] D. J. Lesieutre and J. P. Sullivan, "The analysis of counter-rotating propeller systems," *SAE Transactions*, vol. 94, no. 4, pp. 564–575, 1985.

[39] J. E. Kerwin, "The solution of propeller lifting surface problems by vortex lattice methods," US Department of the Navy, Tech. Rep. AD-262-648, 1961.

[40] A. S. Olsen, "Optimisation of propellers using the vortex-lattice method," Ph.D. dissertation, Technical University of Denmark, 2002.

[41] H. Abedi, L. Davidson, and S. Voutsinas, "Enhancement of free vortex filament method for aerodynamic loads on rotor blades," *Journal of Solar Energy Engineering*, vol. 139, no. 3, 2017.

[42] J. D. Colmenares, O. D. López, and S. Preidikman, "Computational study of a transverse rotor aircraft in hover using the unsteady vortex lattice method," *Mathematical Problems in Engineering*, vol. 2015, 2015.

[43] J. Katz and A. Plotkin, *Low-Speed Aerodynamics*. Cambridge University Press, 2001, 2nd Edition.

[44] R. M. James, "On the remarkable accuracy of the vortex lattice method," *Computer Methods in Applied Mechanics and Engineering*, vol. 1, no. 1, pp. 59–79, 1972.

[45] E. Pistolesi, "Considerations respecting the mutual influence of systems of airfoils," in *Collected Lectures of the 1937 Principal Meeting of the Lilienthal Society*, 1937.

[46] C. E. Lan, "A quasi-vortex-lattice method in thin wing theory," *Journal of Aircraft*, vol. 11, no. 9, pp. 518–527, 1974.

[47] G. R. Hough, "Remarks on vortex-lattice methods," *Journal of Aircraft*, vol. 10, no. 5, pp. 314–317, 1973.

[48] M. Ramasamy, "Contributions to the measurement and analysis of helicopter blade tip vortices," Ph.D. dissertation, University of Maryland, 2004.

[49] S. Ananthan, J. G. Leishman, and M. Ramasamy, "The role of filament stretching in the free-vortex modeling of rotor wakes," in *58th Annual Forum and Technology Display of the Americal Helicopter Society International*, 2002, pp. 11–13.

[50] M. J. Bhagwat and J. G. Leishman, "Correlation of helicopter rotor tip vortex measurements," *AIAA Journal*, vol. 38, no. 2, pp. 301–308, 2000.

[51] J. A. Cole, M. D. Maughmer, G. Bramesfeld, and M. P. Kinzel, "A practical application of an unsteady formulation of the kutta-joukowski theorem," in *35th AIAA Applied Aerodynamics Conference*, AIAA 2017-3904, 2017.

[52] R. J. Simpson, R. Palacios, and J. Murua, "Induced-drag calculations in the unsteady vortex lattice method," *AIAA Journal*, vol. 51, no. 7, pp. 1775–1779, 2013.

[53] T. Lambert and G. Dimitriadis, "Induced drag calculations with the unsteady vortex lattice method for cambered wings," *AIAA Journal*, vol. 55, no. 2, pp. 668–672, 2017.

[54] M. Drela, "Integrated simulation model for preliminary aerodynamic, structural, and control-law design of aircraft," in *40th Structures, Structural Dynamics, and Materials Conference and Exhibit*, 99-1394, 1999.

[55] N. K. Borer, M. D. Patterson, J. K. Viken, M. D. Moore, J. Bevirt, A. M. Stoll, and A. R. Gibson, "Design and performance of the nasa sceptor distributed electric propulsion flight demonstrator," in *16th AIAA Aviation Technology, Integration, and Operations Conference*, AIAA 2016-3920, 2016.

[56] B. L. Litherland, M. D. Patterson, J. M. Derlaga, and N. K. Borer, "A method for designing conforming folding propellers," in *17th AIAA Aviation Technology, Integration, and Operations Conference*, AIAA 2017-3781, 2017.

[57] B. Ortun, R. Boisard, and I. Gonzalez-Martino, "In-plane airloads of a propeller with inflow angle: Prediction vs. experiment," in *30th AIAA Applied Aerodynamics Conference*, AIAA 2012-2778, 2012.

[58] *Openvsp*, Accessed: 18 Jun 2020, 2020.

[59] W. M. Chan, S. A. Pandya, S. E. Rogers, J. C. Jensen, H. C. Lee, D. L. Kao, P. G. Buning, R. L. Meakin, D. A. Boger, and S. M. Nash, *Chimera grid tools user's manual, v.2.2*, 2018.

[60] R. Nichols, R. Tramel, and P. Buning, "Solver and turbulence model upgrades to overflow 2 for unsteady and high-speed applications," in *24th AIAA Applied Aerodynamics Conference, Fluid Dynamics and Co-located Conferences*, AIAA 2006-2824, San Francisco, CA, Jun. 2006.

[61] R. H. Nichols and P. G. Buning, *User's manual for overflow 2.2, v.2.2m*, 2017.

[62] A. K. Henrick, T. D. Aslam, and J. M. Powers, "Mapped weighted essentially non-oscillatory schemes: Achieving optimal order near critical points," *Journal of Computational Physics*, vol. 207, no. 2, pp. 542–567, Aug. 2005.

[63] R. Tramel, R. Nichols, and P. Buning, "Addition of improved shock-capturing schemes to overflow 2.1," in *19th AIAA Computational Fluid Dynamics*, ser. Fluid Dynamics and Co-located Conferences, AIAA 2009-3988, American Institute of Aeronautics and Astronautics, Jun. 2009.

[64] M. L. Shur, M. K. Strelets, A. K. Travin, and P. R. Spalart, "Turbulence modeling in rotating and curved channels: Assessing the spalart-shur correction," *AIAA Journal*, vol. 38, no. 5, pp. 784–792, May 2000.

[65] F. R. Menter, "Two-equation eddy-viscosity turbulence models for engineering applications," *AIAA Journal*, vol. 32, no. 8, pp. 1598–1605, Aug. 1994.

[66] R. Langtry and F. Menter, "Transition modeling for general cfd applications in aeronautics," in *43rd AIAA Aerospace Sciences Meeting and Exhibit*, ser. Aerospace Sciences Meetings, AIAA 2005-522, American Institute of Aeronautics and Astronautics, Jan. 2005.

[67] R. Jain, "Cfd performance and turbulence transition predictions on an installed model-scale rotor in hover," in *55th AIAA Aerospace Sciences Meeting*, AIAA 2017-1871, 2017.

[68] ——, "Hover predictions on the s-76 rotor with tip shape variation using helios," *Journal of Aircraft*, vol. 55, no. 1, pp. 66–77, 2018.

[69] S. Pandya and W. Chan, "Computation of sectional loads from surface triangulation and flow data," in *20th AIAA Computational Fluid Dynamics Conference*, AIAA 2011-3680, 2011.

[70] G. J. Leishman, *Principles of Helicopter Aerodynamics*. Cambridge University Press, 2006.

[71] R. E. Kuhn and W. C. Hayes Jr, "Wind-tunnel investigation of longitudinal aerodynamic characteristics of three propeller-driven vtol configurations in the transition speed range, including effects of ground proximity," National Aeronautics and Space Administration, Tech. Rep. NASA-TN-D-55, 1960.

[72] W. A. Newsom Jr, "Effect of propeller location and flap deflection on the aerodynamic characteristics of a wing-propeller combination for angles of attack from 0 to

80 degrees," National Advisory Committee for Aeronautics, Tech. Rep. NACA-TN-3917, 1957.

[73] ——, "Force-test investigation of the stability and control characteristics of a four-propeller tilt-wing vtol model with a programed flap," National Aeronautics and Space Administration, Tech. Rep. NASA-TN-D-1389, 1962.

[74] ——, "Flight investigation of the longitudinal stability and control characteristics of a four-propeller tilt-wing vtol model with a programed flap," National Aeronautics and Space Administration, Tech. Rep. NASA-TN-D-1390, 1962.

[75] H. L. Kelley, J. P. Reeder, and R. A. Champine, "Summary of a flight-test evaluation of the cl-84 tilt-wing v/stol aircraft," National Aeronautics and Space Administration, Tech. Rep. NASA-TM-X-1914, 1970.

[76] R. J. Pegg, H. L. Kelley, and J. P. Reeder, "Flight investigation of the vz-2 tilt-wing aircraft with full-span flap," National Aeronautics and Space Administration, Tech. Rep. NASA-TN-D-2680, 1965.